

## The FAST Ursa Major cluster HI survey (FUMaS): catalog and HI mass function

HAIYANG YU <sup>1,2,3</sup> MING ZHU <sup>1,2,3,4</sup> CHUAN-PENG ZHANG <sup>1,3,4</sup> PENG JIANG <sup>1,3,4</sup> AND JIN-LONG XU<sup>1,3,4</sup>

<sup>1</sup>*National Astronomical Observatories, Chinese Academy of Sciences, A20 Datun Road, Beijing 100101, China*

<sup>2</sup>*University of Chinese Academy of Sciences, Beijing 100049, China*

<sup>3</sup>*CAS Key Laboratory of FAST, National FAST, National Astronomical Observatories, Chinese Academy of Sciences, Beijing 100101, China*

<sup>4</sup>*Guizhou Radio Astronomical Observatory, Guizhou University, Guiyang 550000, People's Republic of China*

### ABSTRACT

Using the Five-hundred-meter Aperture Spherical radio Telescope (FAST), we have performed an Ursa Major cluster HI Survey (FUMaS) covering the entire UMa region centered at RA=11<sup>h</sup>59<sup>m</sup>28<sup>s</sup>.3, DEC=49°05'18" with a radius of 7.5°. We have obtained the most complete catalog of HI sources in the UMa cluster, containing 179 HI sources with velocities in the range 625-1213.4 km s<sup>-1</sup> and masses in the range 10<sup>6.0</sup>-10<sup>10.1</sup> M<sub>⊙</sub> assuming a distance of 17.4 Mpc. Among them, 55 HI sources were detected for the first time. 32 HI sources do not have optical counterparts with known redshifts, and we found 25 possible counterparts in the multicolor optical image, and another 7 may be HI clouds. We also detected HI distributions in some interacting systems, e.g. the overlapping gas disks between NGC 3992 and its three companion galaxies, filaments around NGC 4026 and NGC 4111, and debris-like gas around NGC 3998. We computed the HIMF of the UMa cluster using the 1/V<sub>max</sub> method and fitting it with the non-linear least squares (NLLS) and modified maximum likelihood (MML) method for the parameters: log<sub>10</sub>(ϕ<sub>\*</sub>/Mpc<sup>-3</sup>) = -0.86 ± 0.18, α = -1.10 ± 0.08 and log<sub>10</sub>(M<sub>\*</sub>/M<sub>⊙</sub>) = 9.92 ± 0.23 for the NLLS method, and log<sub>10</sub>(ϕ<sub>\*</sub>/Mpc<sup>-3</sup>) = -0.78 ± 0.11, α = -1.10 ± 0.05 and log<sub>10</sub>(M<sub>\*</sub>/M<sub>⊙</sub>) = 9.88 ± 0.14 for the MML method. This result is similar to that derived with VLA data, but the slope is steeper at the low-mass end because we detected more low-mass galaxies. The slope is flatter than that of the global HIMF, which is in agreement with the theoretical prediction that galaxies in high-density regions are stripped of gas due to interactions.

### 1. INTRODUCTION

The Lambda Cold Dark Matter (ΛCDM) model of the Universe, validated by many observations, depicts the hierarchical formation of structures of the Universe (White & Rees 1978). In this theoretical framework, small, Gaussian fluctuations are influenced by gravity to form dark matter halos through mergers and accretions. In dark matter halos, the surrounding baryons gradually cool and accrete to form galaxies, groups, clusters, filaments, and other large-scale structures (LSS). Although the ΛCDM model has led to a better understanding of the formation of LSS, the state of the early Universe, and the cosmic abundance of matter and energy, there are still some observational discrepancies that need to be resolved (Bull et al. 2016). For example, the slope

at the low-mass end of the dark-matter halo mass function (Jenkins et al. 2001) is much steeper than that of the galaxy luminosity function (LF, Blanton et al. 2001, 2003) and the neutral hydrogen mass function (HIMF, Zwaan et al. 2005; Jones et al. 2018), i.e., there are a large number of predicted low-mass dark-matter halos that have not been observed. To address this discrepancy, there are two directions of theory, one that modifies the nature of dark matter to suppress the formation of low-mass halos or increases their destruction (Spergel & Steinhardt 2000; Kravtsov et al. 2004), and another that suppresses star formation in low-mass halos so that they are not observed (Verde et al. 2002; Benitez-Llambay & Frenk 2020).

HI is an important component of galaxies, and its 21 cm emission line can provide many additional important parameters for galactic studies. A growing number of HI blind surveys have been conducted to explore the distributional properties of HI sources in the Universe. In contrast to optical and infrared surveys, HI

blind surveys can detect gas-rich, low luminosity, or low surface brightness galaxies that cannot be optically detected. This is a good complement to the detection of low-mass galaxies. HI surveys that have been carried out over large areas of the sky include the HI Parkes All Sky Survey (HIPASS), the Arecibo Legacy Fast ALFA (ALFALFA), and so on (Giovanelli & Haynes 2015). HIPASS covers the entire southern sky area south of the declination  $+2^\circ$  and identified 4315 HI sources. It has a root mean square (RMS) noise of  $13 \text{ mJy beam}^{-1}$  and a velocity range of  $-1280$  to  $127000 \text{ km s}^{-1}$  (Barnes et al. 2001; Meyer et al. 2004). ALFALFA has a higher sensitivity, detecting 31500 HI sources with  $z < 0.06$  over an observation range of 7000 square degrees (Giovanelli et al. 2005; Haynes et al. 2018).

HIMF (Zwaan et al. 2005; Martin et al. 2010; Jones et al. 2018) represents the distribution of the number of galaxies in different mass intervals, and it follows the Schechter equation (Schechter 1976), whose characteristic parameters are the slope  $\alpha$  describing the low-mass end and the characteristic 'knee' mass  $M_*$  at the high-mass end, respectively. The first attempt to derive the HIMF was from Arecibo's blind HI survey. Zwaan et al. (1997) used data from the Arecibo HI Strip Survey, which covered 65 square degrees and contained 66 detections, and measured the slope of the HIMF to be about  $-1.2$ . Rosenberg & Schneider (2002) used the Arecibo Dual-beam Survey data covering an area of approximately 430 square degrees and measured a steeper slope of approximately  $-1.5$ . As more and more large surveys are carried out, the overall distribution of HI in the universe becomes more and more clear. The low-mass slope parameter calculated by HIPASS using 4315 detections is  $-1.37$ , and the 'knee' mass is  $9.80$  (Zwaan et al. 2005). The data from 100% ALFALFA give a slightly different result, with a low mass slope of  $-1.25$  and a 'knee' mass of  $9.94$  (Jones et al. 2018). The current MIGHTEE Early Science data (Maddox et al. 2021), based on the MeerKAT radio interferometer, give the first HIMF based on two different methods:  $1/V_{\text{max}}$  and Modified Maximum Likelihood (MML), whose parameters are  $\alpha = -1.29$ ,  $M_* = 10.07$  for  $1/V_{\text{max}}$  and  $\alpha = -1.44$ ,  $M_* = 10.22$  for MML, respectively (Ponomareva et al. 2023). There is some variability in the present HIMF, which may be due to differences in the observing regions, as the distribution of HI is correlated with the environment and morphology.

Springob et al. (2005) optically selected a large number of spiral galaxies with morphology later than S0a for the study of the effects of morphology and environment on the HIMF. The results show a significant dependence of the HIMF on morphology, with galaxies

with later morphology having steeper low-mass slopes of the HIMF. Higher density regions have a flatter HIMF low-mass slope and lower 'knee' mass, but the variability is insignificant. Zwaan et al. (2003) obtained similar results with the HIMF of the 1000 brightest galaxies from HIPASS, with late-type galaxies having steeper slopes. Moorman et al. (2014) selected about 7300 galaxies from ALFALFA and classified them as void galaxies (low density) versus wall galaxies (high density), with galaxies in the void regions having lower HI mass. Jones et al. (2016) investigated the dependence of the HIMF on the environment using 70% of the ALFALFA data. Their work delineated the surrounding density of galaxies based on the Sloan Digital Sky Survey (SDSS) and 2MASS Redshift Survey (2MRS) catalogs. They found a dependence of the 'knee' mass on the environment, which grew from  $9.81$  to  $10.00$  as the SDSS galaxy density increased. In contrast, the density delineation based on the 2MRS catalogs did not find any dependence on the environment. In addition, the dependence of the low-mass slope on the environment was not found in this work. The HIMF for the Parkes HI Zone of Avoidance (HIZOA) survey shows that the low-mass slope steepens with decreasing density, while there is no clear trend for the 'knee' mass (Said et al. 2019). In addition to the environmental classification of galaxies in large-scale blind surveys, direct observation of targeting specific environments is another way to study the environmental effects on the HIMF. For observations of specific high-density groups and clusters of galaxies, the slopes of most of the HIMFs show a flatter slope (Freeland et al. 2009; Pisano et al. 2011; Westmeier et al. 2017; Busekool et al. 2021) compared to the global HIMF, except for the Leo I group of galaxies, which has a slope of  $-1.41$ , but with a large error ( $\pm 0.2$ ) (Stierwalt et al. 2009). The environment has a strong correlation with HIMF, but the precise regularity remains to be explored.

The Ursa Major (UMa) cluster provides an excellent environment in which to study the influence of the environment on the HIMF. With a distance of  $17.4 \text{ Mpc}$  (Tully & Courtois 2012), this cluster is one of the three moderately sized clusters in the Milky Way neighborhood. However, the cluster has received less attention than the Virgo and Fornax clusters because of its location at the junction of large-scale filamentary structures and the lack of any concentrating core. Tully et al. (1996) first defined the projection of the UMa cluster as being within a circle centered at  $\text{RA}=11^{\text{h}}59^{\text{m}}28^{\text{s}}.3$ ,  $\text{DEC}=49^\circ 05' 18''$ , and with a radius of  $7.5^\circ$ . They identified 79 members with a velocity range of  $700$ - $1210 \text{ km s}^{-1}$  and a small velocity dispersion of  $148 \text{ km s}^{-1}$ . Pak et al. (2014) identified 166 galaxies and

studied their morphological distributions with spectroscopic data from SDSS-DR7 and the NASA/IPAC Extragalactic Database (NED). The result suggests that the UMa cluster is dominated by late-type galaxies, but there are also a large number of early-type galaxies, especially in the dwarf region. Verheijen & Sancisi (2001) studied the HI properties and kinematics of 43 spiral galaxies in UMa with the Westerbork Synthesis Radio Telescope (WSRT). Busekool et al. (2021) calculated the HIMF of the UMa cluster using data from these WSRT observations as well as from a blind HI survey of a 16% region of the UMa cluster with the Very Large Array (VLA). They found a low slope ( $\alpha = -0.92$ ) in the HIMF, which indicates a lack of a gas-rich dwarf galaxies in the UMa cluster. The HI Jodrell All Sky Survey (HIJASS) also conducted a blind survey of the UMa region, but did not cover the complete circular region (Wolfinger et al. 2013). In addition, the work of HIPASS and ALFALFA did not cover the UMa region. So, the study of the UMa cluster lacks a complete catalog of HI sources. The current FAST All Sky HI survey (FASHI) (Zhang et al. 2024) using the Five-hundred-meter Aperture Spherical radio Telescope (FAST) can cover this region completely, and the high sensitivity of FAST can give us a new perspective on the HI distribution of the UMa cluster. A number of HI source detections have been reported in the first data release of FASHI, but data for the UMa cluster are not yet complete due to the schedule-filler observation strategy of the FASHI project. This work was designed to complete the survey of the UMa cluster by make additional observations and data analysis.

In this paper, we present the catalog and HIMF resulting from the FAST UMa cluster HI survey (FUMaS). In Section 2, we describe the observational setup of the project and data processing. Section 3 describes the catalog of the UMa cluster and compares them with existing catalogs. Section 4 discusses HI sources without known-redshift optical counterparts and complexes in the catalog. The calculation of the HIMF is described in Section 5. It is summarized in Section 6.

## 2. OBSERVATIONS AND DATA PROCESSING

### 2.1. Observations

The data used in this paper come from observations made by the FASHI project of FAST in 2021-2023 and additional observations in January 2024. FAST is a single-dish radio telescope with an aperture of 500 m and an illuminating aperture of 300 m located in Guizhou, China (Jiang et al. 2019, 2020; Qian et al. 2020). It has a zenith angle (ZA) of up to  $40^\circ$ , so it can observe over a range of declinations from  $-14.4$  to  $65.6^\circ$ , and covers

a frequency range of 1050-1450 MHz. FASHI is a blind survey of the full sky area within which FAST can observe, and it is expected to detect more than 100000 HI sources over 22000 square degrees. Its first release of the catalog is publicly available, with 41741 HI sources detected over a range of 7600 square degrees (Zhang et al. 2024). Since FASHI is observed in schedule-filler time, it is difficult to control a uniform distribution over the sky area, so we made additional observations of some regions of UMa with the on-the-fly (OTF) mode in January 2024 to ensure that every position in the UMa region has been observed at least twice.

FAST's 19-beam receiver (Dunning et al. 2017) makes blind surveys more efficient and faster. At 1.4 GHz, it has a half-power beamwidth (HPBW) of about  $2.9'$  per beam and a system temperature of about 18 K, which is related to the ZA. The pointing error is less than  $16''$ . The spectral-line backend is used with Spec(W), which provides two linear polarisation information for HI observations. It has 65536 channels in the 500 MHz range, that is, frequency and velocity resolutions up to 7.6 kHz and  $1.6 \text{ km s}^{-1}$ . The observation sampling time is 1 s. For intensity calibration, we used a strong noise diode injected every 32 s during the observation, with a noise diode temperature of about 11 K. The majority of the observing mode in the FASHI project is in drift-scan mode (DecDriftWithAngle). The MultiBeamOTF mode was also combined for directional observations of the UMa region.

### 2.2. Data Processing

Data processing is mainly based on HiFAST pipeline (Jing et al. 2024), which is a dedicated pipeline for processing FAST HI data. Its processing steps are antenna temperature calibration, position determination, flux calibration, baseline removal, radio frequency interference (RFI) flagging, standing-wave removal, Doppler velocity calibration, and gridding. Each step is independently modular, and users can choose to use it according to their needs. Firstly, the antenna temperature calibration is based on the noise diode temperature, which is frequency- and beam-dependent, and converts the machine counts to the antenna temperature. Then the pointing position of each sampling point in the sky is calculated based on the position information of the feed. The flux calibration is obtained by calculating the antenna gain, which is approximately  $16.1 \text{ K Jy}^{-1}$ , which is related to the ZA. For the removal of the baseline, we used the asymmetrically reweighted penalized least-squares (arPLS) algorithm (Baek et al. 2015), which iteratively increases the weight of the signal below the fitted baseline and decreases the weight above it to ob-

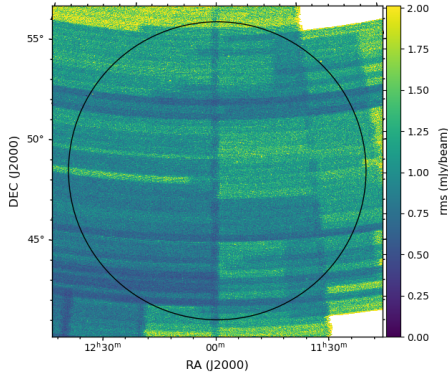


**Figure 1.** RMS distribution of FAST observations of the UMa region. The black circle marks the UMa region with a radius of  $7.5^\circ$ . The mean value of RMS in the region is about  $1 \text{ mJy beam}^{-1}$ .

tain the optimal fitted line. This method is very effective for studying HI emission lines and has performed well in many previous FAST works (Xu et al. 2021; Yu et al. 2023; Zhou et al. 2023). We combined standing-wave removal with the sinusoidal function fitting method in the baseline removal module, which is effective for our data in the short frequency range between 1399-1429 MHz. There is no RFI interference in this range, so we did not use the RFI flagging module. After finally converting the frequencies to heliocentric velocities, we gridded them into a cube with a spatial resolution of  $1'$ . In order to obtain high-quality spectral lines, we also performed a baseline removal and Hanning smoothing of the spectral lines within each pixel using the baseline removal module. The final velocity resolution of our spectra is about  $4.9 \text{ km s}^{-1}$ . Figure 1 shows the distribution of the RMS within the final cube, which has a mean value of approximately  $1 \text{ mJy beam}^{-1}$ . The inhomogeneity of the figure is mainly due to the difference in the number of observations, with a higher number of observations resulting in a lower RMS.

For the extraction of HI sources, we use the HI Source Finding Application (SoFiA) in version 2 (Serra et al. 2015; Westmeier et al. 2021). This is an application that finds and parameterizes HI sources in a 3D spectral line cube. The finding algorithm we used is the Smoothing + Clipping (S+C) algorithm (Serra et al. 2012). The algorithm involves data smoothing of a specified 3D kernel to pick out voxels whose absolute values exceed a certain threshold. We set the threshold at  $4\sigma$ , with  $\sigma$  being the noise value around the detected source. After searching for sources, SoFiA also provides information on the location, spectra, and moment maps of these sources. Although SoFiA can quickly and automatically find HI

sources in 3D data, there will be some fake sources, interferences, confusions, etc. in the results. So manual screening afterward is unavoidable. We performed secondary processing on the sources filtered out by SoFiA, which includes removing the fake sources and interferences among them; fitting the HI sources with busy-functions (Westmeier et al. 2014), calculating the flux, line width, and velocity information of the spectral lines; and distinguishing the single HI sources in the confusions as much as possible.

### 3. THE URSA MAJOR CLUSTER CATALOG

#### 3.1. Selection of Detections

In the data processing described in the previous section, the positional range of the cubes we finished processing with HiFAST was extended outwards by a distance of about 8 degrees from the center of UMa. In order to remove Galactic effects, we intercepted a velocity range of  $100\text{-}2500 \text{ km s}^{-1}$ . Within this range, we used SoFiA combined with manual screening to make a preliminary selection of 318 detections. We then restricted the range to  $7.5$  degrees and selected members of the UMa cluster using a biweighted scale estimator (Beers et al. 1990), a method used in the work of Pak et al. (2014). By iteratively removing galaxies outside the mean velocity of  $2\sigma$  until convergence, we obtained a UMa cluster catalog with 174 detections. Compared to the optical members, we identified 5 additional HI sources, bringing the total number of detections in our catalog to 179. For comparison with previous data, we calculated the Local Group velocities of the detections via the equation:  $V_0 = V_{\text{helio}} + 300\sin l \cos b$ , where  $l$  and  $b$  are Galactic longitude and Galactic latitude, respectively. The Local Group velocity range and dispersion of the detections in our catalog are  $694\text{-}1307 \text{ km s}^{-1}$  and  $\sigma = 152 \text{ km s}^{-1}$ , respectively, as shown in Figure 2. This agrees well with the results of both Tully et al. (1996) and Pak et al. (2014).

#### 3.2. The Ursa Major Cluster Catalog

Table 1 lists 147 HI sources with known-redshift optical counterparts of the UMa cluster, including 141 individual galaxies, 3 binary galaxy confusions, and 3 complexes. The remaining 32 detections without known-redshift optical counterparts are listed in Table 2. Information on each parameter column in the table is described below:

Column 1: The index number of each UMa cluster HI source.

Columns 2 and 3: The positional coordinates of the detections in degrees of right ascension (RA) and declination (DEC) (J2000). The uncertainty is calcu-

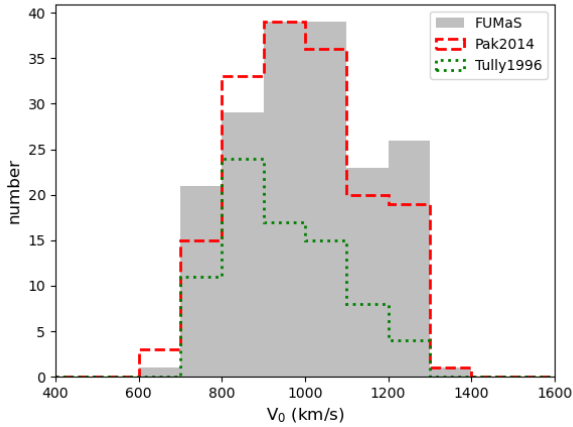


**Figure 2.** Local group velocity distribution of galaxies in the UMA cluster. The grey histogram is from FUMaS, the red dashed line is from Pak et al. (2014), and the green dotted line is from Tully et al. (1996).

lated by the formula (Wolfinger et al. 2013):  $\sigma_{\text{pos}} = \text{HPBW}/(F_{\text{peak}}/\sigma_{\text{rms}})$ , where HPBW is the FAST beam size of  $2.9'$  and  $F_{\text{peak}}$  with  $\sigma_{\text{rms}}$  see columns 7 and 11.

Column 4: Heliocentric velocity of the detections in  $\text{km s}^{-1}$ . The uncertainty is calculated as:  $\sigma_v = 3\sqrt{P\delta v}/\text{SNR}$ , where  $P$  is  $(W_{20} - W_{50})/2$ ,  $\delta v = 4.9 \text{ km s}^{-1}$  is the velocity resolution and SNR is the signal-to-noise ratio as detailed in column 12 (Koribalski et al. 2004).

Column 5: Velocity widths of 50% of the peak intensity of the spectral lines fitted by the busy-function. Its uncertainty is calculated from  $\sigma_{50} = 2\sigma_v$  (Fouque et al. 1990).

Column 6: Velocity widths of 20% of the peak intensity of the spectral lines fitted by the busy-function. Its uncertainty is calculated from  $\sigma_{20} = 3\sigma_v$ .

Column 7: Peak intensity of the spectrum from the busy-function fit in Jy. Uncertainty is  $\sigma_{\text{rms}}$  in column 11.

Column 8: Integrated flux density of the busy-function fitted HI profile in  $\text{Jy km s}^{-1}$ . Subsequent SNR and mass are calculated based on this value.

Column 9: Integrated flux density of the HI profile by summing the fluxes in the same velocity channel as  $S_{\text{bf}}$ .

Column 10: Uncertainty in flux density. Calculated as  $\sigma_s = \sqrt{N}\delta v\sigma_{\text{rms}}$ , where  $N$  is the number of velocity channels. Since the velocity channels of  $S_{\text{bf}}$  and  $S_{\text{sum}}$  are the same, the uncertainties are the same.

Column 11: Noise level of the HI spectrum in Jy at  $4.9 \text{ km s}^{-1}$  spectral resolution. The data used for the calculations are the signal-free spectral line regions.

Column 12: Signal-to-noise ratio of the detections, estimated by the following equation:

$$\text{SNR} = \left(\frac{S_{\text{bf}}}{W_{50}}\right) \frac{w_{\text{sno}}^{1/2}}{\sigma_{\text{rms}}} \quad (1)$$

where  $w_{\text{sno}} = W_{50}/\delta v$  is a smoothing width (Haynes et al. 2018).

Column 13: Logarithm of the detection mass in units of solar mass. Calculated by the following formula:

$$M_{\text{HI}} = 2.356 \times 10^5 D^2 S_{\text{bf}}, \quad (2)$$

where  $D$  is the distance, and due to the uniform distribution of the UMA galaxy cluster, we adopt the average UMA distance of 17.4 Mpc (Tully & Courtois 2012) for all the detections.

Columns 14-17: Information on the optical counterparts of the detections obtained from NED<sup>1</sup> and SDSS DR16 (Ahumada et al. 2020), which are name, RA, DEC, and velocity.

Columns 18: Flags for newly detected HI sources (n), clouds on the outskirts of galaxies (c), sources in the first release of FASHI (f).

<sup>1</sup> <https://ned.ipac.caltech.edu/>

Table 1. FUMaS HI source with known-redshift optical counterpart catalog.

[1]	[2]	[3]	[4]	[5]	[6]	[7]	[8]	[9]	[10]	[11]	[12]	[13]	[14]	[15]	[16]	[17]	[18]
ID	Ra	Dec	$V_{\text{helio}} \pm \sigma_v$	$W_{50} \pm \sigma_{50}$	$W_{20} \pm \sigma_{20}$	$F_{\text{peak}}$	$S_{\text{bf}}$	$S_{\text{sum}}$	$\sigma_s$	$\sigma_{\text{rms}}$	SNR	$\log M$	Opt name	Opt ra	Opt dec	Opt v	Flags
	( $^{\circ}$ )	( $^{\circ}$ )	( $\text{km s}^{-1}$ )	( $\text{km s}^{-1}$ )	( $\text{km s}^{-1}$ )	(Jy)	(Jy)	(Jy)	(Jy)	(Jy)	( $M_{\odot}$ )	( $M_{\odot}$ )		( $^{\circ}$ )	( $^{\circ}$ )	( $\text{km s}^{-1}$ )	
FUMa 001	182.736	50.286	$876.8 \pm 0.12$	$102.2 \pm 0.24$	$115.3 \pm 0.36$	0.061	6.267	6.334	0.0899	0.0021	136.2	8.7	UGC 7176	182.73	50.288	888	f
FUMa 002	182.772	50.486	$772.3 \pm 0.03$	$397.6 \pm 0.06$	$424.3 \pm 0.09$	0.433	117.463	117.866	0.2419	0.0035	768.5	9.9	NGC 4157	182.768	50.485	771	f
FUMa 003	181.354	50.358	$748.8 \pm 0.09$	$278.0 \pm 0.18$	$297.9 \pm 0.27$	0.086	23.182	23.371	0.1616	0.0027	235.9	9.2	NGC 4085	181.345	50.353	760	f
FUMa 004	181.412	50.542	$755.2 \pm 0.03$	$343.7 \pm 0.06$	$373.1 \pm 0.09$	0.438	138.693	138.672	0.2273	0.0035	981.0	10.0	NGC 4088	181.393	50.539	746	f
FUMa 005	180.791	44.532	$703.8 \pm 0.05$	$235.5 \pm 0.1$	$265.6 \pm 0.15$	0.189	41.872	41.764	0.1499	0.0026	469.0	9.5	NGC 4051	180.79	44.531	700	
FUMa 006	171.667	53.747	$643.6 \pm 0.03$	$131.9 \pm 0.06$	$146.4 \pm 0.09$	0.418	44.822	44.987	0.1404	0.003	595.4	9.5	UGC 6446	171.669	53.747	646	
FUMa 007	179.51	51.343	$625.0 \pm 0.43$	$25.5 \pm 0.86$	$40.7 \pm 1.29$	0.032	0.961	0.86	0.0692	0.002	42.9	7.8	SDSS J115802.14+512057.7	179.509	51.349	576	
FUMa 008	180.144	47.772	$660.4 \pm 0.19$	$81.6 \pm 0.38$	$99.1 \pm 0.57$	0.042	3.43	3.509	0.0697	0.0017	103.6	8.4	UGC 262	180.148	47.774	569	n
FUMa 009	186.393	45.684	$714.9 \pm 0.14$	$161.7 \pm 0.28$	$186.4 \pm 0.42$	0.055	8.007	8.025	0.0835	0.0017	171.6	8.8	NGC 4389	186.397	45.685	718	f
FUMa 010	179.741	44.192	$680.9 \pm 0.73$	$68.3 \pm 1.46$	$90.4 \pm 2.19$	0.013	0.732	0.781	0.0528	0.0013	30.1	7.7	CGCG 215-13	179.737	44.193	687	n
FUMa 011	179.626	43.943	$833.0 \pm 0.06$	$392.6 \pm 0.12$	$412.9 \pm 0.18$	0.162	41.391	41.402	0.2017	0.0029	325.3	9.5	NGC 4013	179.63	43.947	831	
FUMa 012	184.181	46.079	$704.4 \pm 0.11$	$140.3 \pm 0.22$	$153.0 \pm 0.33$	0.063	7.356	7.414	0.091	0.0019	149.2	8.7	UGC 7301	184.175	46.079	706	f
FUMa 013	184.05	47.876	$948.2 \pm 0.39$	$338.2 \pm 0.78$	$356.6 \pm 1.17$	0.02	3.346	3.506	0.1038	0.0016	51.7	8.4	NGC 4220	184.049	47.883	914	f
FUMa 014	183.944	48.129	$725.3 \pm 0.1$	$109.0 \pm 0.2$	$154.3 \pm 0.3$	0.076	8.468	8.388	0.0506	0.0011	324.8	8.8	NGC 4218	183.943	48.131	730	f
FUMa 015	180.684	45.191	$711.5 \pm 0.35$	$158.5 \pm 0.7$	$169.0 \pm 1.05$	0.012	1.437	1.502	0.0592	0.0012	43.5	8.0	UGC 7022	180.682	45.191	709	n
FUMa 016	178.772	44.102	$647.5 \pm 1.24$	$25.8 \pm 2.48$	$34.7 \pm 3.72$	0.005	0.126	0.103	0.0274	0.001	11.3	7.0	SDSS J115506.03+440611.7	178.775	44.103	628	n
FUMa 017	178.42	47.857	$803.1 \pm 0.03$	$259.1 \pm 0.06$	$287.7 \pm 0.09$	0.202	44.316	44.49	0.0929	0.0016	791.3	9.5	NGC 3949	178.424	47.859	794	f
FUMa 018	175.327	46.399	$753.1 \pm 0.16$	$85.1 \pm 0.32$	$112.5 \pm 0.48$	0.056	4.803	4.814	0.065	0.0015	152.4	8.5	CGCG 242-075	175.342	46.393	746	
FUMa 019	174.83	46.511	$734.7 \pm 0.04$	$90.7 \pm 0.08$	$132.3 \pm 0.12$	0.44	41.399	40.951	0.1201	0.0028	697.5	9.5	NGC 3782	174.836	46.514	733	
FUMa 020	174.945	46.618	$711.0 \pm 0.2$	$42.1 \pm 0.4$	$68.9 \pm 0.6$	0.027	1.272	1.244	0.0315	0.0007	119.9	8.0	SDSS J113948.69+463711.4	174.953	46.62	712	
FUMa 021	179.904	42.953	$679.2 \pm 0.56$	$55.1 \pm 1.12$	$74.9 \pm 1.68$	0.01	0.58	0.576	0.0359	0.0009	37.3	7.6	SDSS J115936.94+425715.7	179.904	42.954	668	n
FUMa 022	177.149	43.724	$739.2 \pm 0.28$	$135.8 \pm 0.56$	$150.1 \pm 0.84$	0.026	2.889	2.875	0.0862	0.0018	62.3	8.3	UGC 6776	177.149	43.721	738	
FUMa 023	176.477	50.201	$753.0 \pm 0.14$	$96.2 \pm 0.28$	$135.2 \pm 0.42$	0.089	8.722	8.716	0.0804	0.0019	215.7	8.8	NGC 3870	176.486	50.2	754	
FUMa 024	184.385	47.994	$694.6 \pm 0.29$	$37.6 \pm 0.58$	$57.3 \pm 0.87$	0.023	0.916	0.966	0.0342	0.0009	72.1	7.8	2MASX J12173195+4759420	184.383	47.995	687	f
FUMa 025	181.613	52.702	$846.4 \pm 0.2$	$303.4 \pm 0.4$	$344.1 \pm 0.6$	0.038	11.47	11.432	0.1236	0.002	150.8	8.9	NGC 4102	181.596	52.711	785	f
FUMa 026	179.964	55.665	$736.5 \pm 0.44$	$115.9 \pm 0.88$	$129.0 \pm 1.32$	0.015	1.751	1.761	0.087	0.0019	38.7	8.1	UGC 6988	179.965	55.665	732	
FUMa 027	179.377	55.425	$829.8 \pm 0.85$	$138.8 \pm 1.7$	$222.6 \pm 2.55$	0.019	2.97	2.92	0.1266	0.0023	50.2	8.3	NGC 3990	179.398	55.459	690	
FUMa 028	179.523	55.458	$1207.0 \pm 0.64$	$297.7 \pm 1.28$	$337.7 \pm 1.92$	0.01	2.408	2.337	0.1042	0.0014	46.0	8.2	NGC 3998	179.484	55.454	1020	
FUMa 029	178.939	55.321	$835.1 \pm 0.08$	$253.3 \pm 0.16$	$278.5 \pm 0.24$	0.111	17.855	17.923	0.0988	0.0017	298.8	9.1	NGC 3972	178.938	55.321	842	
FUMa 030	179.119	55.119	$1112.2 \pm 0.06$	$212.2 \pm 0.12$	$245.1 \pm 0.18$	0.151	28.601	28.919	0.1144	0.0021	425.7	9.3	NGC 3982	179.117	55.125	1122	f
FUMa 031	180.079	50.653	$743.8 \pm 0.42$	$126.8 \pm 0.84$	$140.2 \pm 1.26$	0.014	1.413	1.415	0.0645	0.0014	41.2	8.0	UGC 6992	180.079	50.653	759	
FUMa 032	179.327	49.28	$777.3 \pm 0.02$	$121.6 \pm 0.04$	$137.6 \pm 0.06$	0.393	42.575	42.759	0.1066	0.0023	759.3	9.5	UGC 6930	179.322	49.283	777	
FUMa 033	173.341	47.029	$862.0 \pm 0.04$	$269.7 \pm 0.08$	$290.9 \pm 0.12$	0.545	111.991	112.843	0.3871	0.0064	479.9	9.9	NGC 3726	173.338	47.029	864	f

Table 1 continued

Table 1 (continued)

[1]	[2]	[3]	[4]	[5]	[6]	[7]	[8]	[9]	[10]	[11]	[12]	[13]	[14]	[15]	[16]	[17]	[18]
ID	Ra	Dec	$V_{\text{helio}} \pm \sigma_v$	$W_{50} \pm \sigma_{50}$	$W_{20} \pm \sigma_{20}$	$F_{\text{peak}}$	$S_{\text{bf}}$	$S_{\text{sum}}$	$\sigma_s$	$\sigma_{\text{rms}}$	SNR	$\log M$	Opt name	Opt ra	Opt dec	Opt v	Flags
	( $^\circ$ )	( $^\circ$ )	( $\text{km s}^{-1}$ )	( $\text{km s}^{-1}$ )	( $\text{km s}^{-1}$ )	(Jy)	(Jy)	(Jy)	(Jy)	(Jy)	( $M_\odot$ )	( $M_\odot$ )		( $^\circ$ )	( $^\circ$ )	( $\text{km s}^{-1}$ )	
FUMa 034	185.07	45.902	$730.9 \pm 0.13$	$67.2 \pm 0.26$	$80.1 \pm 0.39$	0.043	2.719	2.779	0.0476	0.0012	125.0	8.3	UGC 7391	185.068	45.908	737	f
FUMa 035	170.84	50.891	$791.1 \pm 0.1$	$173.9 \pm 0.2$	$186.7 \pm 0.3$	0.083	11.941	11.956	0.1291	0.0025	164.1	8.9	UGC 6399	170.847	50.893	791	f
FUMa 036	182.895	47.655	$742.5 \pm 0.44$	$80.1 \pm 0.88$	$93.3 \pm 1.32$	0.014	1.087	1.085	0.06	0.0014	38.5	7.9	SDSS J121134.99+473927.1	182.896	47.658	752	f
FUMa 037	185.198	47.826	$742.6 \pm 0.22$	$52.7 \pm 0.44$	$68.0 \pm 0.66$	0.049	2.297	2.29	0.0655	0.0017	82.7	8.2	UGC 7401	185.202	47.826	762	f
FUMa 038	178.812	44.151	$726.4 \pm 0.32$	$41.4 \pm 0.64$	$52.5 \pm 0.96$	0.033	1.358	1.427	0.0724	0.002	48.2	8.0	KDG 081	178.808	44.15	27	f
FUMa 039	176.532	47.492	$887.4 \pm 0.08$	$334.5 \pm 0.16$	$356.1 \pm 0.24$	0.125	25.762	25.854	0.1526	0.0023	272.1	9.3	NGC 3877	176.532	47.495	895	f
FUMa 040	182.371	43.685	$888.0 \pm 0.24$	$261.3 \pm 0.48$	$341.8 \pm 0.72$	0.102	26.648	26.391	0.2545	0.0043	174.2	9.3	NGC 4138	182.374	43.685	874	f
FUMa 041	183.232	52.264	$781.8 \pm 0.17$	$99.5 \pm 0.34$	$120.7 \pm 0.51$	0.049	4.753	4.779	0.0754	0.0017	126.4	8.5	UGC 7218	183.237	52.265	770	f
FUMa 042	177.693	45.806	$805.0 \pm 0.09$	$154.2 \pm 0.18$	$173.7 \pm 0.27$	0.115	16.161	16.19	0.132	0.0027	222.2	9.1	UGC 6818	177.696	45.807	808	f
FUMa 043	178.21	44.121	$808.2 \pm 0.02$	$92.7 \pm 0.04$	$109.6 \pm 0.06$	1.098	94.685	95.66	0.173	0.004	1109.6	9.8	NGC 3938	178.206	44.121	808	f
FUMa 044	173.454	53.121	$1045.3 \pm 0.19$	$230.1 \pm 0.38$	$249.8 \pm 0.57$	0.037	5.451	5.513	0.0861	0.0015	107.6	8.6	NGC 3729	173.456	53.126	1000	f
FUMa 045	173.154	53.072	$987.1 \pm 0.03$	$459.6 \pm 0.06$	$478.5 \pm 0.09$	0.659	176.544	177.016	0.3412	0.0046	808.8	10.1	NGC 3718	173.145	53.068	993	f
FUMa 046	185.08	48.139	$797.3 \pm 0.13$	$125.5 \pm 0.26$	$139.9 \pm 0.39$	0.035	3.957	3.966	0.0537	0.0011	139.5	8.5	UGC 7392	185.073	48.137	808	f
FUMa 047	179.204	50.815	$890.0 \pm 0.09$	$131.2 \pm 0.18$	$141.8 \pm 0.27$	0.106	10.939	11.117	0.1257	0.0027	162.8	8.9	UGC 6922	179.217	50.817	877	f
FUMa 048	179.969	50.499	$939.3 \pm 0.27$	$81.1 \pm 0.54$	$92.8 \pm 0.81$	0.017	1.317	1.336	0.0461	0.0011	59.5	8.0	SDSS J115950.81+502955.3	179.962	50.499	876	n
FUMa 049	174.948	54.513	$795.1 \pm 0.59$	$108.5 \pm 1.18$	$121.0 \pm 1.77$	0.014	1.101	1.141	0.076	0.0017	28.2	7.9	SDSS J113948.41+543116.0	174.952	54.521	790	f
FUMa 050	179.659	47.259	$901.5 \pm 0.04$	$263.9 \pm 0.08$	$283.3 \pm 0.12$	0.182	42.798	42.908	0.1527	0.0026	463.7	9.5	NGC 4010	179.658	47.261	902	f
FUMa 051	178.856	54.657	$847.1 \pm 0.26$	$127.0 \pm 0.52$	$145.1 \pm 0.78$	0.041	4.971	4.927	0.1204	0.0026	77.6	8.5	UGC 6894	178.848	54.657	850	f
FUMa 052	177.188	49.359	$800.7 \pm 0.7$	$37.7 \pm 1.4$	$58.1 \pm 2.1$	0.021	0.863	0.889	0.0753	0.0021	30.3	7.8	SDSS J114845.15+492129.6	177.188	49.358	798	n
FUMa 053	179.551	48.882	$820.5 \pm 0.26$	$79.4 \pm 0.32$	$92.7 \pm 0.78$	0.032	2.501	2.522	0.0782	0.0019	66.4	8.3	MCG +08-22-048	179.548	48.882	833	f
FUMa 054	177.408	48.416	$961.9 \pm 0.11$	$35.7 \pm 0.22$	$52.8 \pm 0.33$	0.162	6.045	6.011	0.0969	0.0027	169.5	8.6	NGC 3906	177.419	48.426	959	f
FUMa 055	177.389	44.398	$795.4 \pm 0.78$	$32.6 \pm 1.56$	$47.2 \pm 2.34$	0.013	0.433	0.446	0.0528	0.0015	22.9	7.5	SDSS J114930.92+442433.1	177.379	44.409	802	n
FUMa 056	177.708	48.249	$807.8 \pm 1.45$	$52.6 \pm 2.9$	$69.3 \pm 4.35$	0.005	0.23	0.2	0.0405	0.0011	13.2	7.2	Mrk 1460	177.709	48.251	810	f
FUMa 057	179.938	53.62	$1138.9 \pm 0.64$	$27.8 \pm 1.28$	$48.0 \pm 1.92$	0.014	0.438	0.475	0.0394	0.0011	33.0	7.5	SDSS J115943.26+533638.9	179.93	53.611	1132	f
FUMa 058	175.157	46.124	$885.9 \pm 0.78$	$41.8 \pm 1.56$	$70.9 \pm 2.34$	0.011	0.537	0.542	0.0433	0.0012	32.3	7.6	SDSS J114035.57+460727.5	175.148	46.124	888	f
FUMa 059	175.029	45.936	$849.0 \pm 0.02$	$39.6 \pm 0.04$	$54.4 \pm 0.06$	0.694	27.682	28.023	0.0796	0.0022	913.3	9.3	UGC 6628	175.024	45.943	849	f
FUMa 060	181.665	54.764	$846.9 \pm 0.16$	$86.2 \pm 0.32$	$96.9 \pm 0.48$	0.033	2.855	2.884	0.0603	0.0015	95.6	8.3	SDSS J120637.89+544557.7	181.658	54.766	850	f
FUMa 061	179.124	50.426	$914.1 \pm 0.05$	$188.0 \pm 0.1$	$202.8 \pm 0.15$	0.213	30.565	30.732	0.1515	0.0029	353.1	9.3	UGC 6917	179.11	50.429	911	f
FUMa 062	179.709	46.464	$819.2 \pm 0.35$	$30.3 \pm 0.7$	$47.7 \pm 1.05$	0.025	0.817	0.815	0.0421	0.0012	56.2	7.8	SDSS J115849.68+462753.0	179.707	46.465	792	n
FUMa 063	183.319	43.7	$931.7 \pm 0.02$	$234.0 \pm 0.04$	$246.6 \pm 0.06$	0.31	48.953	49.195	0.1031	0.0018	799.6	9.5	NGC 4183	183.32	43.699	929	f
FUMa 064	177.691	51.824	$955.7 \pm 0.04$	$278.2 \pm 0.08$	$291.8 \pm 0.12$	0.16	28.86	28.901	0.1029	0.0019	406.9	9.3	NGC 3917	177.69	51.825	965	f
FUMa 065	177.478	51.739	$946.2 \pm 0.75$	$41.8 \pm 1.5$	$60.5 \pm 2.25$	0.007	0.3	0.297	0.0471	0.0008	27.1	7.3	SBS 1147+520	177.477	51.736	938	f
FUMa 066	177.703	56.459	$881.8 \pm 0.1$	$117.2 \pm 0.2$	$132.9 \pm 0.3$	0.161	14.846	14.866	0.1583	0.0035	179.5	9.0	UGC 6816	177.698	56.455	894	f
FUMa 067	169.245	50.589	$847.6 \pm 0.33$	$57.1 \pm 0.66$	$75.4 \pm 0.99$	0.023	1.327	1.247	0.0379	0.0013	60.6	8.0	CGCG 268-012	169.251	50.585	860	n
FUMa 068	181.451	50.794	$827.2 \pm 1.27$	$28.5 \pm 2.54$	$43.3 \pm 3.81$	0.005	0.146	0.154	0.0288	0.0009	14.2	7.0	SDSS J120549.54+504729.0	181.456	50.791	827	n
FUMa 069	178.455	52.331	$1048.8 \pm 0.04$	$407.5 \pm 0.08$	$424.0 \pm 0.12$	0.202	52.217	52.344	0.1676	0.0024	491.7	9.6	NGC 3953	178.454	52.327	1050	f

Table 1 continued

Table 1 (*continued*)

[1]	[2]	[3]	[4]	[5]	[6]	[7]	[8]	[9]	[10]	[11]	[12]	[13]	[14]	[15]	[16]	[17]	[18]
ID	Ra	Dec	$V_{\text{helio}} \pm \sigma_v$	$W_{50} \pm \sigma_{50}$	$W_{20} \pm \sigma_{20}$	$F_{\text{peak}}$	$S_{\text{bf}}$	$S_{\text{sum}}$	$\sigma_s$	$\sigma_{\text{rms}}$	SNR	$\log M$	Opt name	Opt ra	Opt dec	Opt v	Flags
	( $^{\circ}$ )	( $^{\circ}$ )	( $\text{km s}^{-1}$ )	( $\text{km s}^{-1}$ )	( $\text{km s}^{-1}$ )	(Jy)	(Jy)	(Jy)	(Jy)	(Jy)	(M $_{\odot}$ )	(M $_{\odot}$ )		( $^{\circ}$ )	( $^{\circ}$ )	( $\text{km s}^{-1}$ )	
FUMa 070	178.04	52.11	$1017.0 \pm 0.04$	$140.4 \pm 0.08$	$153.9 \pm 0.12$	0.134	16.378	16.385	0.0694	0.0014	435.7	9.1	UGC 6840	178.03	52.108	1015	
FUMa 071	183.967	47.091	$1029.2 \pm 0.05$	$387.6 \pm 0.1$	$404.7 \pm 0.15$	0.121	32.363	32.397	0.1248	0.0018	411.4	9.4	NGC 4217	183.962	47.092	1028	f
FUMa 072	178.487	50.173	$854.8 \pm 1.14$	$45.1 \pm 2.28$	$54.9 \pm 3.42$	0.006	0.255	0.19	0.0487	0.0013	12.9	7.3	UGC 6874	178.491	50.18	869	n
FUMa 073	176.105	48.834	$899.2 \pm 0.06$	$91.2 \pm 0.12$	$104.1 \pm 0.18$	0.206	16.852	17.021	0.1177	0.0027	292.5	9.1	UGC 6713	176.104	48.836	899	
FUMa 074	178.391	45.906	$860.1 \pm 0.55$	$25.3 \pm 1.1$	$49.0 \pm 1.65$	0.027	0.85	0.858	0.0638	0.0018	41.4	7.8	SDSS J115332.97+455421.8	178.387	45.906	802	n
FUMa 075	179.18	48.335	$952.2 \pm 0.08$	$127.4 \pm 0.16$	$172.2 \pm 0.24$	0.16	20.605	20.448	0.1038	0.0022	372.7	9.2	NGC 3985	179.175	48.334	983	
FUMa 076	179.868	42.359	$888.3 \pm 0.3$	$50.3 \pm 0.6$	$77.3 \pm 0.9$	0.021	1.116	1.104	0.0338	0.0009	81.1	7.9	KUG 1156+426	179.872	42.349	885	n
FUMa 077	171.765	51.073	$872.4 \pm 0.78$	$34.6 \pm 1.56$	$45.2 \pm 2.34$	0.009	0.324	0.326	0.0449	0.0013	19.6	7.4	SDSS J112705.35+510428.9	171.772	51.075	886	n
FUMa 078	185.782	53.015	$890.7 \pm 0.44$	$43.1 \pm 0.88$	$63.8 \pm 1.32$	0.015	0.651	0.64	0.0347	0.0009	48.1	7.7	SDSS J122307.98+530120.6	185.784	53.022	894	f
FUMa 079	181.536	49.581	$1077.3 \pm 0.05$	$371.6 \pm 0.1$	$395.2 \pm 0.15$	0.228	48.955	49.021	0.1695	0.0025	461.1	9.5	NGC 4100	181.536	49.583	1074	f
FUMa 080	183.906	44.282	$895.0 \pm 0.38$	$59.0 \pm 0.76$	$74.2 \pm 1.14$	0.019	1.143	1.153	0.0355	0.0014	47.8	7.9	SDSS J121537.12+441710.0	183.905	44.286	892	f
FUMa 081	177.007	49.804	$923.2 \pm 0.17$	$95.0 \pm 0.34$	$107.1 \pm 0.51$	0.072	6.651	6.627	0.1404	0.0033	94.9	8.7	UGC 6773	177.001	49.808	924	
FUMa 082	176.362	48.488	$883.5 \pm 0.92$	$36.7 \pm 1.84$	$51.6 \pm 2.76$	0.009	0.336	0.358	0.0448	0.0013	19.7	7.4	SDSS J114525.71+482906.8	176.357	48.485	892	n
FUMa 083	181.604	42.435	$879.0 \pm 0.84$	$44.9 \pm 1.68$	$58.2 \pm 2.52$	0.006	0.254	0.256	0.0302	0.0008	20.3	7.3	SDSS J120625.35+422604.7	181.606	42.435	886	f
FUMa 084	178.914	56.249	$951.1 \pm 0.68$	$123.6 \pm 1.36$	$160.9 \pm 2.04$	0.017	2.095	2.034	0.0956	0.002	41.8	8.2	SBS 1153+565	178.905	56.253	948	
FUMa 085	183.518	53.747	$898.9 \pm 0.44$	$36.3 \pm 0.88$	$55.9 \pm 1.32$	0.025	0.968	0.958	0.0553	0.0015	47.2	7.8	SBS 1211+540	183.51	53.755	903	f
FUMa 086	179.012	52.444	$879.7 \pm 0.7$	$33.5 \pm 1.4$	$41.8 \pm 2.1$	0.007	0.221	0.219	0.0308	0.0009	19.3	7.2	SDSS J115603.70+522618.3	179.015	52.438	875	n
FUMa 087	175.609	51.594	$975.5 \pm 0.09$	$181.3 \pm 0.18$	$193.4 \pm 0.27$	0.09	11.639	11.697	0.1077	0.0021	189.3	8.9	UGC 6667	175.61	51.598	973	
FUMa 088	174.434	54.041	$893.8 \pm 1.33$	$48.7 \pm 2.66$	$75.5 \pm 3.99$	0.004	0.228	0.209	0.029	0.0008	18.3	7.2	2MASX J11374447+5402441	174.435	54.046	896	
FUMa 089	177.076	56.328	$1081.1 \pm 0.45$	$19.9 \pm 0.9$	$30.4 \pm 1.35$	0.032	0.669	0.635	0.0679	0.002	33.8	7.7	SDSS J114820.16+562045.7	177.084	56.346	1030	n
FUMa 090	177.303	56.095	$1158.5 \pm 0.12$	$468.7 \pm 0.24$	$488.6 \pm 0.36$	0.174	45.753	46.011	0.4181	0.0056	170.8	9.5	NGC 3898	177.314	56.085	1162	f
FUMa 091	177.379	56.028	$921.2 \pm 1.25$	$24.0 \pm 2.5$	$31.8 \pm 3.75$	0.003	0.077	0.074	0.0195	0.0007	10.5	6.7	SDSS J114929.60+560154.1	177.374	56.032	904	n
FUMa 092	182.751	52.834	$914.4 \pm 1.05$	$47.0 \pm 2.1$	$75.6 \pm 3.15$	0.009	0.443	0.431	0.0455	0.0012	23.9	7.5	SBS 1208+531	182.753	52.833	911	f
FUMa 093	175.885	55.48	$967.6 \pm 0.21$	$146.0 \pm 0.42$	$155.6 \pm 0.63$	0.039	4.92	4.972	0.1286	0.0026	70.0	8.5	UGC 6685	175.88	55.479	974	
FUMa 094	180.251	49.912	$936.4 \pm 0.22$	$66.4 \pm 0.44$	$76.2 \pm 0.66$	0.031	1.832	1.848	0.0604	0.0015	67.9	8.1	UGC 6999	180.255	49.913	912	
FUMa 095	177.665	55.359	$950.8 \pm 0.06$	$42.3 \pm 0.12$	$57.3 \pm 0.18$	0.032	13.706	13.947	0.1103	0.003	316.2	9.0	NGC 3913	177.662	55.354	955	
FUMa 096	176.61	53.408	$917.2 \pm 1.83$	$28.6 \pm 3.66$	$36.3 \pm 5.49$	0.003	0.087	0.072	0.0343	0.001	7.1	6.8	SDSS J114628.27+532443.4	176.618	53.412	926	n
FUMa 097	177.956	48.69	$983.7 \pm 0.21$	$67.6 \pm 0.42$	$96.4 \pm 0.63$	0.139	9.275	9.162	0.1695	0.0042	121.3	8.8	NGC 3928	177.948	48.683	978	
FUMa 098	177.227	47.581	$958.0 \pm 0.48$	$29.5 \pm 0.96$	$48.7 \pm 1.44$	0.028	0.907	0.818	0.0631	0.0018	43.0	7.8	SDSS J114855.43+473457.5	177.231	47.583	963	
FUMa 099	182.984	46.976	$974.0 \pm 0.46$	$98.0 \pm 0.92$	$113.3 \pm 1.38$	0.011	0.894	0.891	0.0446	0.001	40.0	7.8	MCG +08-22-083	182.982	46.982	985	f
FUMa 100	184.824	44.799	$936.1 \pm 1.1$	$41.9 \pm 2.2$	$56.7 \pm 3.3$	0.004	0.149	0.141	0.0219	0.0006	16.4	7.0	SDSS J121915.07+444801.8	184.813	44.801	922	f
FUMa 101	177.753	47.942	$945.6 \pm 1.12$	$32.4 \pm 2.24$	$37.7 \pm 3.36$	0.005	0.134	0.138	0.0381	0.0011	9.6	7.0	SDSS J115059.60+475749.4	177.749	47.963	942	
FUMa 102	182.695	45.722	$943.2 \pm 0.65$	$14.3 \pm 1.3$	$33.0 \pm 1.95$	0.011	0.217	0.217	0.0276	0.0008	31.1	7.2	LEDA 2832109	182.694	45.724	959	f
FUMa 103	182.369	54.936	$967.7 \pm 0.59$	$39.8 \pm 1.18$	$58.8 \pm 1.77$	0.02	0.814	0.818	0.0611	0.0017	34.9	7.8	SDSS J120931.73+545618.1	182.383	54.939	995	f
FUMa 104	178.161	50.039	$999.9 \pm 0.16$	$76.5 \pm 0.32$	$99.1 \pm 0.48$	0.095	6.491	6.419	0.0997	0.0024	139.6	8.7	UGC 6849	178.163	50.038	1003	
FUMa 105	179.193	49.026	$981.0 \pm 0.52$	$48.4 \pm 1.04$	$69.4 \pm 1.56$	0.016	0.817	0.827	0.0478	0.0013	41.3	7.8	SDSS J115644.29+490118.2	179.185	49.022	984	n

Table 1 (*continued*)



Table 1 (*continued*)

[1]	[2]	[3]	[4]	[5]	[6]	[7]	[8]	[9]	[10]	[11]	[12]	[13]	[14]	[15]	[16]	[17]	[18]
ID	Ra	Dec	$V_{\text{helio}} \pm \sigma_v$	$W_{50} \pm \sigma_{50}$	$W_{20} \pm \sigma_{20}$	$F_{\text{peak}}$	$S_{\text{bf}}$	$S_{\text{sum}}$	$\sigma_s$	$\sigma_{\text{rms}}$	SNR	$\log M$	Opt name	Opt ra	Opt dec	Opt v	Flags
	( $^{\circ}$ )	( $^{\circ}$ )	( $\text{km s}^{-1}$ )	( $\text{km s}^{-1}$ )	( $\text{km s}^{-1}$ )	(Jy)	(Jy)	(Jy)	(Jy)	(Jy)		( $M_{\odot}$ )		( $^{\circ}$ )	( $^{\circ}$ )	( $\text{km s}^{-1}$ )	
FUMa 106	183.284	44.09	957.5 $\pm$ 1.23	35.9 $\pm$ 2.46	50.0 $\pm$ 3.69	0.005	0.182	0.155	0.0331	0.001	14.3	7.1	SDSS J121255.18+440527.3	183.23	44.091	969	f
FUMa 107	179.788	52.702	1083.1 $\pm$ 0.02	173.8 $\pm$ 0.04	189.0 $\pm$ 0.06	0.333	44.072	44.208	0.0876	0.0017	892.5	9.5	UGC 6983	179.791	52.707	1081	f
FUMa 108	176.553	54.169	984.0 $\pm$ 0.7	30.6 $\pm$ 1.4	33.9 $\pm$ 2.1	0.004	0.1	0.1	0.0223	0.0007	12.2	6.9	SDSS J114613.44+541034.3	176.556	54.176	996	
FUMa 109	178.955	45.168	1037.6 $\pm$ 0.32	77.1 $\pm$ 0.64	106.9 $\pm$ 0.96	0.045	3.483	3.436	0.0932	0.0023	79.7	8.4	SDSS J115551.80+450945.5	178.966	45.163	1048	n
FUMa 110	178.676	46.604	1004.2 $\pm$ 0.61	32.7 $\pm$ 1.22	46.5 $\pm$ 1.83	0.01	0.347	0.351	0.0324	0.001	28.7	7.4	SDSS J115441.22+463636.2	178.672	46.61	1009	
FUMa 111	180.845	43.741	1042.5 $\pm$ 0.41	71.2 $\pm$ 0.82	87.5 $\pm$ 1.23	0.013	0.919	0.979	0.0431	0.0011	46.0	7.8	2MASX J12032304+4344395	180.846	43.744	1063	
FUMa 112	182.451	43.234	1061.8 $\pm$ 0.1	71.1 $\pm$ 0.2	83.9 $\pm$ 0.3	0.052	3.59	3.781	0.0446	0.0011	173.8	8.4	UGC 7146	182.455	43.235	1065	f
FUMa 113	176.639	55.826	1074.7 $\pm$ 0.37	76.4 $\pm$ 0.74	88.2 $\pm$ 1.11	0.014	1.038	1.051	0.05	0.0012	43.9	7.9	SDSS J114634.04+554916.6	176.642	55.822	1079	
FUMa 114	176.395	55.887	1151.5 $\pm$ 0.08	171.5 $\pm$ 0.16	186.3 $\pm$ 0.24	0.079	10.061	10.124	0.0837	0.0016	212.6	8.9	NGC 3850	176.398	55.887	1159	
FUMa 115	170.255	53.17	1156.5 $\pm$ 0.03	100.6 $\pm$ 0.06	124.6 $\pm$ 0.09	0.636	57.401	57.878	0.159	0.0036	711.1	9.6	NGC 3631	170.262	53.17	1151	f
FUMa 116	173.761	54.846	1182.8 $\pm$ 0.02	235.8 $\pm$ 0.04	249.3 $\pm$ 0.06	0.472	79.84	79.992	0.1567	0.0027	861.4	9.8	NGC 3733	173.757	54.851	1184	f
FUMa 117	180.255	55.024	1110.4 $\pm$ 0.34	95.6 $\pm$ 0.68	107.5 $\pm$ 1.02	0.014	1.109	1.148	0.046	0.0011	48.1	7.9	MCG +09-20-063	180.252	55.026	1133	n
FUMa 118	182.375	53.103	1165.2 $\pm$ 0.08	178.3 $\pm$ 0.16	194.1 $\pm$ 0.24	0.107	15.954	16.038	0.1154	0.0022	244.3	9.1	NGC 4142	182.376	53.105	1158	f
FUMa 119	182.483	42.498	1094.4 $\pm$ 1.43	126.8 $\pm$ 2.86	170.2 $\pm$ 4.29	0.003	0.411	0.315	0.037	0.0008	21.6	7.5	NGC 4143	182.4	42.534	946	f
FUMa 120	179.994	49.565	1133.7 $\pm$ 0.25	85.3 $\pm$ 0.5	100.5 $\pm$ 0.75	0.028	2.395	2.394	0.0682	0.0016	72.3	8.2	MCG +08-22-051	179.99	49.564	1124	
FUMa 121	182.054	55.748	1121.8 $\pm$ 1.39	50.5 $\pm$ 2.78	74.0 $\pm$ 4.17	0.012	0.611	0.575	0.0858	0.0024	16.3	7.6	SDSS J120810.72+554447.2	182.045	55.746	1111	f
FUMa 122	170.983	52.921	1213.4 $\pm$ 0.06	197.6 $\pm$ 0.12	216.9 $\pm$ 0.18	0.274	42.974	43.22	0.2266	0.0042	326.5	9.5	NGC 3657	170.982	52.921	1217	
FUMa 123	177.549	42.071	1126.6 $\pm$ 1.26	92.8 $\pm$ 2.52	126.7 $\pm$ 3.78	0.003	0.242	0.253	0.0185	0.0005	21.6	7.2	UGC 6805	177.551	42.074	1158	
FUMa 124	180.874	55.05	1119.0 $\pm$ 1.55	32.4 $\pm$ 3.1	90.4 $\pm$ 4.65	0.004	0.172	0.141	0.0197	0.0006	23.0	7.1	SDSS J120330.64+550306.0	180.878	55.052	1113	
FUMa 125	177.976	53.103	1121.2 $\pm$ 0.54	32.4 $\pm$ 1.08	50.3 $\pm$ 1.62	0.009	0.313	0.304	0.0244	0.0007	36.6	7.3	SDSS J115153.66+530558.2	177.974	53.1	1124	
FUMa 126	177.733	48.533	1138.4 $\pm$ 0.45	68.3 $\pm$ 0.9	86.7 $\pm$ 1.35	0.015	1.036	1.075	0.0517	0.0013	44.2	7.9	SDSS J115056.11+483153.6	177.734	48.532	1127	
FUMa 127	174.719	43.165	1197.5 $\pm$ 0.15	160.2 $\pm$ 0.3	179.1 $\pm$ 0.45	0.044	6.083	6.135	0.0818	0.0016	133.7	8.6	UGC 6611	174.714	43.165	1192	
FUMa 128	179.715	45.731	1149.7 $\pm$ 0.1	40.5 $\pm$ 0.2	58.9 $\pm$ 0.3	0.151	6.345	6.499	0.0801	0.0022	205.8	8.7	UGCA 259	179.719	45.734	1154	
FUMa 129	173.016	53.736	1136.2 $\pm$ 1.47	22.1 $\pm$ 2.94	51.7 $\pm$ 4.41	0.007	0.186	0.168	0.035	0.001	17.3	7.1	SDSS J113202.25+534418.2	173.01	53.738	1138	n
FUMa 130	179.891	54.226	1141.2 $\pm$ 0.57	19.8 $\pm$ 1.14	31.1 $\pm$ 1.71	0.018	0.384	0.338	0.0475	0.0014	27.8	7.4	SDSS J115934.75+541317.9	179.895	54.222	1155	n
FUMa 131	183.235	53.463	1156.0 $\pm$ 0.72	34.0 $\pm$ 1.44	50.1 $\pm$ 2.16	0.01	0.344	0.353	0.0362	0.001	26.0	7.4	SBS 1210+537A	183.233	53.461	1155	f
FUMa 132	184.494	46.932	1153.6 $\pm$ 1.37	50.3 $\pm$ 2.74	68.1 $\pm$ 4.11	0.004	0.197	0.174	0.0308	0.0009	14.4	7.1	SDSS J121759.40+465634.3	184.498	46.943	1149	f
FUMa 133	179.067	51.283	1160.0 $\pm$ 0.86	29.4 $\pm$ 1.72	36.3 $\pm$ 2.58	0.011	0.277	0.335	0.0566	0.0016	14.4	7.3	SDSS J115616.24+511706.9	179.068	51.285	1159	n
FUMa 134	179.998	44.716	1171.2 $\pm$ 0.41	52.5 $\pm$ 0.82	66.9 $\pm$ 1.23	0.017	0.856	0.901	0.0464	0.0012	43.5	7.8	PGC 166118	179.995	44.718	1168	
FUMa 135	174.887	43.412	1159.1 $\pm$ 1.05	38.0 $\pm$ 2.1	44.8 $\pm$ 3.15	0.004	0.147	0.187	0.032	0.0009	11.6	7.0	SDSS J113930.28+432428.5	174.876	43.408	1153	n
FUMa 136	177.865	49.789	1197.1 $\pm$ 0.59	41.9 $\pm$ 1.18	55.2 $\pm$ 1.77	0.017	0.704	0.742	0.0622	0.0017	28.9	7.7	SDSS J115126.75+494734.4	177.861	49.793	1196	n
Binary galaxy confusion																	
FUMa 137	179.699	42.725	727.7 $\pm$ 0.09	352.1 $\pm$ 0.18	384.6 $\pm$ 0.27	0.129	34.085	34.301	0.1783	0.0027	307.0	9.4	UGC 6973 - UGC 6962				
FUMa 138	174.437	47.895	740.3 $\pm$ 0.07	229.0 $\pm$ 0.14	257.3 $\pm$ 0.21	0.406	69.447	69.69	0.334	0.0059	351.5	9.7	NGC 3769 - NGC 3769A				f
FUMa 139	177.166	48.695	969.0 $\pm$ 0.05	262.8 $\pm$ 0.1	307.8 $\pm$ 0.15	0.432	113.673	113.535	0.3204	0.0054	588.3	9.9	NGC 3893 - NGC 3896				f
Complex																	

Table 1 (*continued*)

Table 1 (*continued*)

[1]	[2]	[3]	[4]	[5]	[6]	[7]	[8]	[9]	[10]	[11]	[12]	[13]	[14]	[15]	[16]	[17]	[18]
ID	Ra	Dec	$V_{\text{helio}} \pm \sigma_v$	$W_{50} \pm \sigma_{50}$	$W_{20} \pm \sigma_{20}$	$F_{\text{peak}}$	$S_{\text{bf}}$	$S_{\text{sum}}$	$\sigma_s$	$\sigma_{\text{rms}}$	SNR	$\log M$	Opt name	Opt ra	Opt dec	Opt v	Flags
	( $^{\circ}$ )	( $^{\circ}$ )	( $\text{km s}^{-1}$ )	( $\text{km s}^{-1}$ )	( $\text{km s}^{-1}$ )	(Jy)	(Jy)	(Jy)	(Jy)	(Jy)		( $M_{\odot}$ )		( $^{\circ}$ )	( $^{\circ}$ )	( $\text{km s}^{-1}$ )	
FUMa 140	181.697	43.01	$809.9 \pm 0.2$	$217.2 \pm 0.4$	$260.1 \pm 0.6$	0.27	51.018	50.927	0.5795	0.0104	150.5	9.6	N4111 complex				f
FUMa 141	179.718	50.859	$935.1 \pm 0.14$	$64.6 \pm 0.28$	$110.6 \pm 0.42$	0.33	24.941	27.723	0.3055	0.006	233.3	9.3	NGC4026 complex				f
FUMa 142	179.403	53.35	$1045.9 \pm 0.05$	$469.6 \pm 0.1$	$478.9 \pm 0.15$	0.253	118.898	119.682	0.6353	0.0085	293.2	9.9	NGC3992 complex				f
Galaxy identified by optical comparison																	
FUMa 143	177.799	52.021	$967.4 \pm 1.55$	$28.0 \pm 3.1$	$31.8 \pm 4.65$	0.002	0.05	0.06	0.0226	0.0007	5.9	6.6	NGC 3931	177.806	52.001	914	
FUMa 144	176.97	53.839	$1090.5 \pm 1.4$	$17.1 \pm 2.8$	$36.2 \pm 4.2$	0.006	0.137	0.103	0.036	0.001	14.6	7.0	SDSS J114751.35+535047.9	176.964	53.847	1020	
FUMa 145	180.05	53.502	$1054.6 \pm 0.91$	$3.4 \pm 1.82$	$33.9 \pm 2.73$	0.011	0.086	0.059	0.0214	0.0007	28.5	6.8	2MASX J11595620+5329451	179.984	53.496	1066	
FUMa 146	183.971	47.511	$687.9 \pm 1.4$	$19.3 \pm 2.8$	$34.5 \pm 4.2$	0.002	0.052	0.058	0.011	0.0004	13.1	6.6	SDSS J121551.55+473016.8	183.965	47.505	655.0	n
FUMa 147	187.812	44.757	$962.7 \pm 1.63$	$29.7 \pm 3.26$	$32.5 \pm 4.89$	0.001	0.015	0.01	0.0062	0.0003	4.8	6.0	SDSS J123106.05+4444449.1	187.775	44.747	948.0	n

**Table 2.** FUMaS H I source without known-redshift optical counterpart catalog.

[1]	[2]	[3]	[4]	[5]	[6]	[7]	[8]	[9]	[10]	[11]	[12]	[13]	[14]	[15]	[16]	[17]	[18]
ID	Ra	Dec	$V_{\text{helio}} \pm \sigma_v$	$W_{50} \pm \sigma_{50}$	$W_{20} \pm \sigma_{20}$	$F_{\text{peak}}$	$S_{\text{bf}}$	$S_{\text{aum}}$	$\sigma_s$	$\sigma_{\text{rms}}$	SNR	$\log M$	Opt name	Opt ra	Opt dec	Opt v	Flags
	( $^{\circ}$ )	( $^{\circ}$ )	( $\text{km s}^{-1}$ )	( $\text{km s}^{-1}$ )	( $\text{km s}^{-1}$ )	(Jy)	(Jy)	(Jy)	(Jy)	(Jy)	( $M_{\odot}$ )	( $M_{\odot}$ )		( $^{\circ}$ )	( $^{\circ}$ )	( $\text{km s}^{-1}$ )	
FUMa 148	179.697	55.594	1090.2 $\pm$ 1.55	31.2 $\pm$ 3.1	50.9 $\pm$ 4.65	0.006	0.206	0.197	0.0303	0.0012	13.4	7.2	MATLAS 1137	179.706	55.588		n
FUMa 149	177.47	46.529	714.0 $\pm$ 1.04	30.3 $\pm$ 2.08	39.1 $\pm$ 3.12	0.006	0.148	0.134	0.03	0.0009	13.4	7.0	SDSS J114953.15+463058.9	177.471	46.516		n
FUMa 150	182.324	43.944	893.4 $\pm$ 0.6	16.5 $\pm$ 1.2	30.2 $\pm$ 1.8	0.008	0.148	0.194	0.0207	0.0006	29.1	7.0					cf
FUMa 151	173.043	53.455	717.9 $\pm$ 1.12	28.1 $\pm$ 2.24	36.3 $\pm$ 3.36	0.006	0.179	0.196	0.043	0.0013	12.0	7.1					nc
FUMa 152	175.142	48.257	732.1 $\pm$ 0.73	20.5 $\pm$ 1.46	37.8 $\pm$ 2.19	0.012	0.331	0.283	0.0421	0.0012	26.6	7.4	SMDG J1140318+481531	175.131	48.259		n
FUMa 153	178.304	48.184	759.7 $\pm$ 0.63	19.2 $\pm$ 1.26	34.8 $\pm$ 1.89	0.018	0.393	0.433	0.0455	0.0014	29.5	7.4	SDSS J115311.14+481119.2	178.296	48.189		n
FUMa 154	174.765	45.954	785.8 $\pm$ 0.59	19.6 $\pm$ 1.18	28.8 $\pm$ 1.77	0.007	0.141	0.15	0.0198	0.0006	24.1	7.0	SDSS J113901.68+455721.6	174.757	45.956		n
FUMa 155	178.002	52.551	1044.3 $\pm$ 1.34	25.4 $\pm$ 2.68	36.7 $\pm$ 4.02	0.007	0.168	0.139	0.0529	0.0013	11.8	7.1					nc
FUMa 156	176.183	45.017	817.5 $\pm$ 1.23	17.3 $\pm$ 2.46	30.9 $\pm$ 3.69	0.006	0.128	0.123	0.0319	0.001	14.1	7.0	SMDG J1144447+450018	176.186	45.005		n
FUMa 157	172.487	52.878	861.6 $\pm$ 0.72	26.7 $\pm$ 1.44	36.1 $\pm$ 2.16	0.007	0.198	0.257	0.0292	0.0009	20.0	7.1	SMDG J1129572+525248	172.488	52.88		n
FUMa 158	187.525	50.091	885.4 $\pm$ 0.82	43.2 $\pm$ 1.64	67.8 $\pm$ 2.46	0.007	0.33	0.385	0.0295	0.0008	28.2	7.4	SDSS J123006.79+500525.8	187.528	50.091		n
FUMa 159	179.6	55.071	878.6 $\pm$ 1.3	32.9 $\pm$ 2.6	50.7 $\pm$ 3.9	0.004	0.138	0.159	0.0252	0.0007	15.2	7.0	SDSS J115824.37+550418.2	179.602	55.072		n
FUMa 160	185.41	52.384	881.8 $\pm$ 1.03	26.7 $\pm$ 2.06	36.3 $\pm$ 3.09	0.005	0.14	0.131	0.0296	0.0009	14.1	7.0	SDSS J122139.96+522317.9	185.417	52.388		n
FUMa 161	182.552	43.383	880.7 $\pm$ 1.22	27.5 $\pm$ 2.44	47.0 $\pm$ 3.66	0.005	0.145	0.141	0.0251	0.0007	16.9	7.0					nc
FUMa 162	178.509	47.521	937.6 $\pm$ 0.77	27.1 $\pm$ 1.54	55.7 $\pm$ 2.31	0.012	0.394	0.402	0.0365	0.0011	32.4	7.4	SDSS J115400.21+473056.0	178.501	47.516		n
FUMa 163	182.364	43.199	945.2 $\pm$ 0.46	61.8 $\pm$ 0.92	71.8 $\pm$ 1.38	0.012	0.76	0.755	0.0438	0.0014	32.4	7.7					cf
FUMa 164	181.261	43.233	923.4 $\pm$ 0.7	13.1 $\pm$ 1.4	21.0 $\pm$ 2.1	0.009	0.132	0.126	0.0286	0.0009	18.7	7.0					cf
FUMa 165	178.362	54.201	955.1 $\pm$ 0.56	44.2 $\pm$ 1.12	58.0 $\pm$ 1.68	0.012	0.532	0.53	0.043	0.0012	31.3	7.6					n
FUMa 166	179.618	48.964	957.8 $\pm$ 0.78	22.9 $\pm$ 1.56	35.7 $\pm$ 2.34	0.01	0.247	0.278	0.0366	0.0011	21.6	7.2	SMDG J1158259+485737	179.608	48.96		n
FUMa 167	184.89	43.793	962.8 $\pm$ 0.31	20.9 $\pm$ 0.62	33.0 $\pm$ 0.93	0.016	0.373	0.381	0.0234	0.0007	53.4	7.4	SDSS J121933.46+434706.0	184.889	43.785		f
FUMa 168	178.827	46.318	977.9 $\pm$ 0.77	27.5 $\pm$ 1.54	42.3 $\pm$ 2.31	0.009	0.268	0.274	0.0335	0.001	23.3	7.3	SMDG J1155176+461858	178.823	46.316		n
FUMa 169	182.009	50.899	1026.3 $\pm$ 0.85	38.2 $\pm$ 1.7	53.2 $\pm$ 2.55	0.008	0.293	0.276	0.0359	0.001	21.4	7.3	SDSS J120804.62+505355.1	182.019	50.899		f
FUMa 170	175.012	49.092	1018.7 $\pm$ 0.83	27.8 $\pm$ 1.66	40.6 $\pm$ 2.49	0.007	0.205	0.213	0.0309	0.0009	20.1	7.2	SDSS J114000.43+490606.6	175.002	49.102		n
FUMa 171	181.381	51.552	1020.6 $\pm$ 0.64	22.5 $\pm$ 1.28	24.8 $\pm$ 1.92	0.007	0.151	0.163	0.043	0.0013	11.1	7.0	SDSS J120536.49+513259.7	181.402	51.55		f
FUMa 172	176.734	48.08	1042.9 $\pm$ 0.77	68.1 $\pm$ 1.54	75.8 $\pm$ 2.31	0.005	0.257	0.261	0.0295	0.0008	16.8	7.3	SDSS J114649.67+480530.5	176.707	48.092		n
FUMa 173	186.89	51.037	1049.8 $\pm$ 0.64	30.8 $\pm$ 1.28	48.6 $\pm$ 1.92	0.013	0.452	0.472	0.0418	0.0012	31.0	7.5	SDSS J122731.01+510131.0	186.879	51.025		f
FUMa 174	177.642	49.114	1042.5 $\pm$ 1.58	30.4 $\pm$ 3.16	35.5 $\pm$ 4.74	0.004	0.088	0.068	0.0342	0.0011	6.7	6.8	SDSS J115034.34+490650.1	177.643	49.114		n
FUMa 175	179.993	55.899	1062.8 $\pm$ 1.15	17.2 $\pm$ 2.3	68.1 $\pm$ 3.45	0.015	0.319	0.286	0.0404	0.0012	29.1	7.4					n
FUMa 176	179.876	55.832	1089.5 $\pm$ 0.98	16.7 $\pm$ 1.96	29.3 $\pm$ 2.94	0.006	0.123	0.114	0.0266	0.0008	16.9	6.9	SDSS J115929.42+554946.3	179.873	55.83		n
FUMa 177	178.096	52.348	1117.8 $\pm$ 0.68	17.1 $\pm$ 1.36	43.0 $\pm$ 2.04	0.011	0.249	0.254	0.0257	0.0008	35.1	7.2					nc
FUMa 178	178.259	48.815	1152.7 $\pm$ 0.75	31.1 $\pm$ 1.5	39.4 $\pm$ 2.25	0.009	0.239	0.248	0.0368	0.0011	17.9	7.2	SMDG J1153036+484844	178.265	48.812		n
FUMa 179	178.622	53.35	1165.0 $\pm$ 1.45	15.9 $\pm$ 2.9	42.1 $\pm$ 4.35	0.006	0.123	0.102	0.0278	0.0008	16.6	6.9	SMDG J1154306+532048	178.627	53.347		n

### 3.3. Compare with Previous Catalogs

The first large UMA catalog was built by Tully et al. (1996), containing 79 galaxies, and 70 have HI detections. Compared to these 79 galaxies, we detected HI signals for 77 of these sources, except for 1136+46 and NGC 4346. Note that UGC 7129 has a projected distance of 7.53 degrees from the center of the UMA cluster, which is not included in our catalog. Due to the large gas disks and low resolution of radio telescopes compared to optical instruments, HI sources are subject to confusion, i.e., one HI source corresponds to more than one optical source. In particular, there are six galaxies in three binary galaxy systems which are marked as confusions (UGC 6962/6973, NGC 3769/3769A, and NGC 3893/3896) in our catalog (they are also in the catalog of Tully et al. (1996)). There are four galaxies (NGC 3992, UGC 6923, UGC 6940, and UGC 6969) in the NGC 3992 complex, two galaxies (NGC 4026 and UGC 6956) in the NGC 4026 complex, and six galaxies (NGC 4111, NGC 4117, NGC 4118, UGC 7089, UGC 7094, and 1203+43) in the NGC 4111 complex.

To study the statistical properties of the Tully-Fisher relation and the dark-matter halos around galaxies, Verheijen & Sancisi (2001) selected 43 spiral galaxies from the UMA members with suitable inclinations to be observed with the WSRT and studied their HI properties and dynamics. Busekool et al. (2021) conducted a blind survey of the UMA region using the VLA, consisting of 54 cross-patterned points covering 16% of the area. The table in the article lists 43 galaxies. These sources are all in our catalog. The work of Wolfinger et al. (2013) conducted a blind survey of the UMA region using the 76.2m Lovell telescope at Jodrell Bank Observatory, UK. This work had a detection range of 480 square degrees covering a portion of the UMA region defined by Tully et al. (1996). From their 166 HI signals, we have selected 53 sources within the UMA range of this paper, including 3 new sources that they have confirmed using the Green Bank Telescope (GBT) follow-up observations. These 53 sources all have counterparts in our catalog.

In Figure 3 we compare the position of the HI sources in Table 4 of Busekool et al. (2021), and the 53 sources in HIJASS, with their counterparts in our catalog. For the data in Busekool et al. (2021) Table 4, we filter out the sources that are in complexes and outside the UMA region, leaving 13 sources for comparison, denoted by a cross sign in Figure 3. The comparison of the 53 sources of HIJASS is indicated by dots in Figure 3. In the comparison with HIJASS, there are some cases of large positional gaps, which may be due to the low spatial resolution of the single-antenna telescope. To compare flux and velocity widths, we filter out 9 sources in the

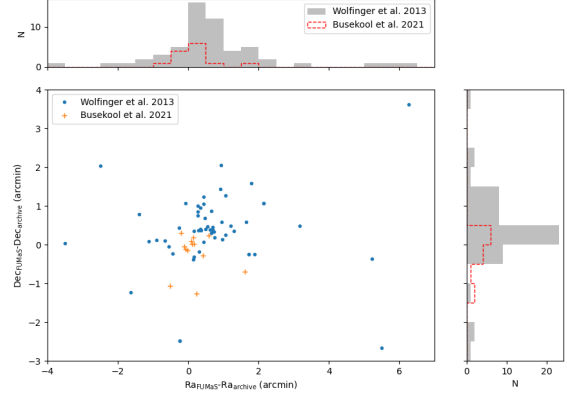


**Figure 3.** Comparison with HI sources location information from previous HI blind survey. HIJASS is marked with ‘.’ and Busekool et al. (2021) is marked with ‘+’. The histogram above shows the distribution of Ra discrepancies, and the distribution of Dec discrepancies is shown on the right.

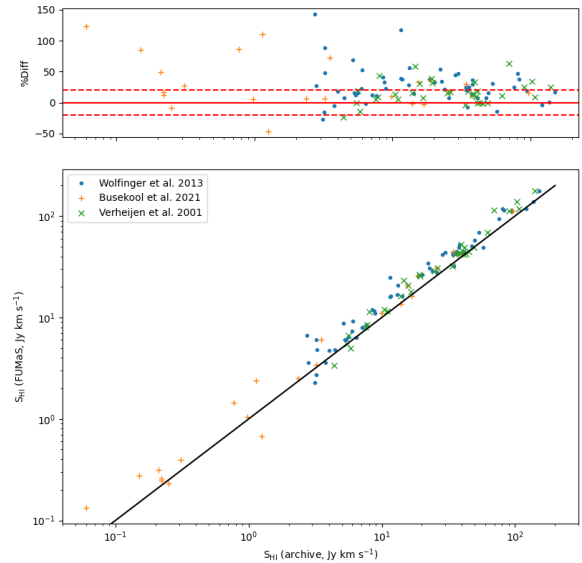


**Figure 4.** Comparison with flux densities in the literature. The upper plot shows the distribution of percent difference, with the horizontal straight line being 0 and the two dashed lines representing  $\pm 20$ . The lower plot compares flux densities, with the diagonal line representing the case where the two are equal. Data in different literature are labeled with different symbols, see figure legend for details.

complexes and select 34 sources in Verheijen & Sancisi (2001). Sources in Busekool et al. (2021) with inaccurate information, e.g. those on the edges of observed region, in complexes, and out of the UMA region are filtered, leaving 23 sources for comparison. The formula for cal-

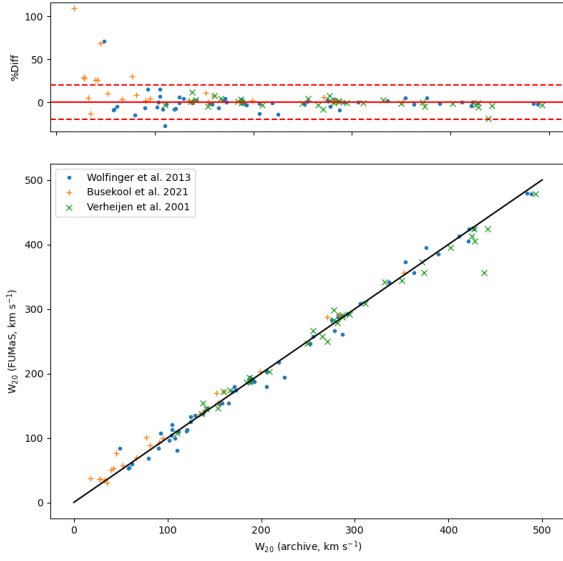


**Figure 5.** Comparison with the 20% velocity width in the literature. The upper plot shows the percentage distribution of the difference. Horizontal lines correspond to 0 and  $\pm 20$ , respectively. The lower plot is a comparison of the data, and the corresponding symbols for the different literature data are indicated in the legend. The diagonal line indicates the consistency of the data.

culating the percentage difference in Figure 4, Figure 5 and Figure 6 is as follows:

$$\text{Difference}\% = \frac{\text{DATA}_{\text{FUMaS}} - \text{DATA}_{\text{archive}}}{\text{DATA}_{\text{archive}}} \times 100, \quad (3)$$

where DATA stands for flux density, 20 percent and 50 percent velocity widths. Figure 4 shows a comparison of the flux densities, where the FUMaS data are generally larger, probably because of the presence of more extended sources in the UMa region. In previous work, it has been shown that FAST observations of extended sources can observe more HI gas and obtain higher flux densities (Xu et al. 2021; Yu et al. 2023; Zhou et al. 2023). The velocity width comparisons show good agreement in Figure 5 and Figure 6. Most of the data differences are in  $\pm 20\%$ .

For the optical counterparts, we compared the sources in Pak et al. (2014). This work confirms 166 galaxies in the UMa cluster using SDSS-DR7 and NED spectroscopic data. They found that while the UMa cluster is dominated by late-type galaxies, it has a significant number of early-type galaxies. In the primary comparison, HI signals were detected for 147 optical galaxies. We then reconfirmed the spectra at locations where no signal was detected and identified 4 HI sources (SDSS J114751.35+535047.9, 2MASX

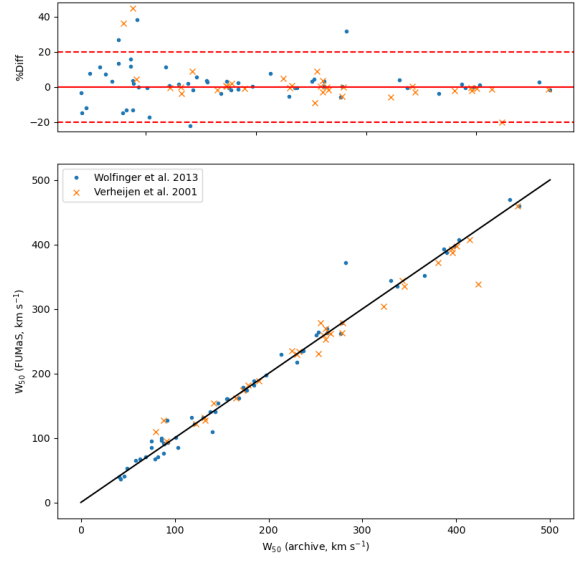


**Figure 6.** Comparison with the 50% velocity width in the literature. The upper plot shows the percentage distribution of the difference. Horizontal lines correspond to 0 and  $\pm 20$ , respectively. The lower plot is a comparison of the data, and the corresponding symbols for the different literature data are indicated in the legend. The diagonal line indicates the consistency of the data.

J11595620+5329451, SDSS J121551.55+473016.8 and SDSS J123106.05+444449.1). As a result, we detected HI signals in 151 of the 166 galaxies in the optical catalog, and 15 did not.

In comparison with previous HI detection works in the UMa region, new sources detected by blind surveys in both VLA and HIJASS have been included in our catalog, proving the high completeness of our work. In comparison with the optical work, we have obtained 5 more detections from optically selected positions. They are listed at the end of Table 1, FUMa 143 to FUMa 147. Finally, our catalog extends to 179 detections, of which 147 have known-redshift optical counterparts and 32 do not. There are 58 HI sources published in the first release of FASHI, and they are flagged with 'f' in the catalog. In addition to the blind surveys mentioned above, there are a number of optically selected observations that provide information on HI in the UMa cluster (Paturel et al. 2003; Huchtmeier et al. 2007; Courtois & Tully 2015; van Driel et al. 2016; Poulain et al. 2022; O'Neil et al. 2023; Chandola et al. 2024). For comparison, there are 55 HI sources in the FUMaS catalog that have been detected for the first time and are flagged with 'n'. Figure 7 shows the moment-0 map for the UMa region with an integrated range of 500-1500 km s<sup>-1</sup>, with detections in

our catalog labeled as red hollow circles, optical galaxies in Pak et al. (2014) labeled as blue crosses, and 3 boxes for regions of the complexes. The size of the marker is proportional to the HI mass and r magnitude. The HI mass and stellar mass distribution of the FUMaS detections are shown in Figure 8. The stellar mass is calculated by the mass-to-light ratio equation (Bell et al. 2003):  $\log_{10}(M/L_r) = -0.306 + 1.097(g - r)$ . As expected, galaxies in the UMa cluster are influenced by their environment, and the HI mass of dwarf galaxies is lower relative to the average value of the FASHI global distribution. The  $M_{\text{HI}}/M_*$  ratios for the UMa galaxies are in general lower than that of the main sequence galaxies. The newly detected HI sources in FUMaS correspond to low-mass galaxies, and those without known-redshift optical counterparts correspond to even lower-mass galaxies. This demonstrate that high sensitivity observations with FAST are crucial in revealing the environmental effects in high density environments.

## 4. DISCUSSION AND RESULTS

### 4.1. HI sources without known-redshift optical counterparts

Thanks to the high sensitivity of FAST, we can detect more low-mass HI sources, with the lowest mass of HI source in the catalog at  $10^{6.0} M_{\odot}$ . There are 55 HI sources in our catalog that are new detections, which are labeled as red circles with crosses in Figure 7. They have masses in the range of  $10^{6.0}$ - $10^{8.4} M_{\odot}$ . In addition, 32 HI sources have no redshift from optical spectra. These sources have masses in the range of  $10^{6.8}$ - $10^{7.7} M_{\odot}$ , and they may be dwarf galaxies or pure HI clouds. For 25 of them, we found possible optical counterparts in optical images. The optical images are from the DESI Survey website<sup>2</sup>, and the center of the images is the center of the HI sources with a size of about  $3 \times 3$  arcmin<sup>2</sup>, which corresponds to the HPBW of FAST. Their multicolor optical images, HI moment-0 maps, and spectral line profiles are shown in Figure 9. Seven of these HI sources (FUMa 152, FUMa 156, FUMa 157, FUMa 166, FUMa 168, FUMa 178 and FUMa 179) correspond to ultra-diffuse galaxies (UDG) in the Systematically Measuring Ultra-diffuse Galaxies (SMUDGes) catalog (Zaritsky et al. 2023). Sixteen HI sources appear to have optical counterparts, and we have labeled them in Figure 9 and listed the related information obtained from NED or SDSS DR16. FUMa 165 and FUMa 175 also have possible optical counterparts but have not been included in any catalogs. These two galaxies are first discovered by

our HI survey. The UDG galaxy UMa 165 appears to be confused with a bright galaxies MCG +09-20-024 with a redshift of 0.06. FUMa 175 seems to be a UDG as well, but its surface brightness is very low so it hasn't been noticed before. The remaining 7 HI sources do not have obvious optical counterparts in the optical images. However, these sources are all close to other galaxies with optical counterparts, so they have a high probability of being HI clouds. Deep multi-wavelength follow-up observations are needed to reveal the nature of these HI sources.

### 4.2. Complexes

Interactions between galaxies are common in galaxy clusters and provide important information for studying the formation and evolution of galaxies. There are many interacting systems in the UMa cluster, such as binary confusions and complexes in the catalog. Some of the interacting galaxy systems have been mentioned in previous papers, such as NGC 4085/4088, NGC 3718/3729, and the NGC 3998 system (Verheijen & Sancisi 2001; Wolfinger et al. 2013). We then describe in detail the distribution of HI in the three complexes in the catalog, as well as in the NGC 3998 system.

NGC 3992 is a barred spiral galaxy. It has three companion galaxies, UGC 6969, UGC 6940 and UGC 6923. Previous HI observations have shown that the gas kinematics of NGC 3992 are very regular and that there is a lack of HI gas in the central bar region. The gas disks of the three companion galaxies are as large as the optical disks and do not appear to overlap (Gottesman et al. 1984; Bottema & Verheijen 2002; Bottema 2002). Figure 10 shows the HI column density contours from FAST observations overlaid on a Digitized Sky Survey (DSS<sup>3</sup>) b-band image, with an integration range of 500-1500 km s<sup>-1</sup> and column density contours starting at  $6 \times 10^{18}$  cm<sup>-2</sup>. The regular distribution of the contours suggests that there does not appear to be a strong interaction between NGC 3992 and its three companion galaxies. The gas disks of the three companion galaxies show irregularities only in UGC 6940, which has a tail to the northeast. Due to the overlap of the gas disks, we can obtain approximate flux densities and masses for the galaxies, which are given in Table 3.

NGC 4026 is one of the three brightest lenticular galaxies in the UMa cluster. Previous large beam-size single-dish telescopes have obtained a large gaseous envelope containing numerous galaxies in this region, including NGC 4026, UGC 6956, UGC 6922, UGC 6917,

<sup>2</sup> <https://www.legacysurvey.org/viewer>

<sup>3</sup> <https://archive.eso.org/dss/dss>

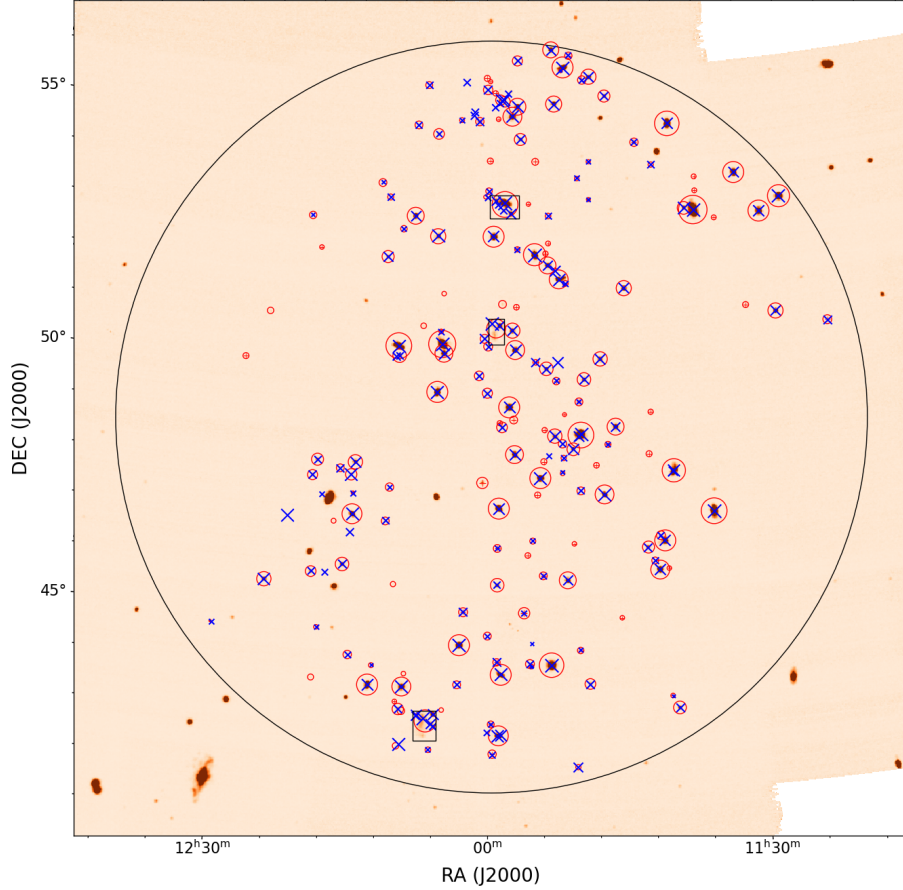


**Figure 7.** Moment-0 map of the UMa region for the  $500\text{-}1500\text{ km s}^{-1}$  integral range. The black circle shows the range of the UMa region. Red circles mark the positions of detections in the FUMaS catalog, with the crosses being the first detected HI sources. The blue crosses are optical galaxies in Pak et al. (2014). Boxes mark the positions of the complexes. The size of the marker is proportional to the HI mass and  $r$  magnitude.

and UGC 6992 (Appleton 1983; Wolfinger et al. 2013). However, the FAST observations are more consistent with previous radio interferometer arrays and there is no apparent interaction between UGC 6956, UGC 6922, and UGC 6917 (van Driel et al. 1988). There is a tail structure to the southwest of UGC 6956 that appears to extend towards UGC 6922, as shown in Figure 11. There is a filament that extends from north of the optical center of N4026 all the way south to near the SDSS J115950.81+502955.3. It has a projected length of about  $28'$ , corresponding to  $142\text{ kpc}$ , and a flux density of about  $11.67\text{ Jy}$ , corresponding to a mass of  $8.3 \times 10^8 M_{\odot}$ . The approximate flux densities and masses of NGC 4026 and UGC 6956 are given in Table 3.

NGC 4111 is also one of the three brightest lenticular galaxies. It is surrounded by several companion galaxies, with NGC 4117 and NGC 4118 to the east and UGC 7089, UGC 7094, and SDSS J120559.63+425409.1 to the west. A little further away are UGC 7146, NGC 4143, and SDSS J120625.35+422604.7. The system has a distinct filament that extends southwards from NGC 4111 and appears to extend southeastwards to near NGC 4143. This filament has a projection of up to  $30'$ , corresponding to a length of  $152\text{ kpc}$ . NGC 4143 has no HI gas in its optical position, but it has two clumps of gas at its southeast and northwest ends, which may represent preexisting gas stripped out by internal or external influences. The properties of the galaxies in this system are also listed in Table 3.

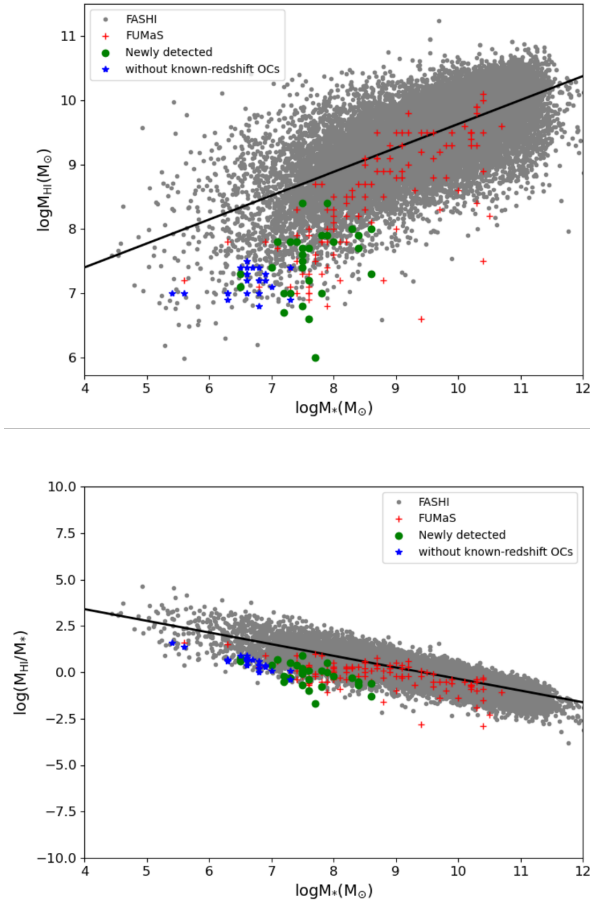


**Figure 8.** HI mass and stellar mass distribution of FUMaS detections. The top panel is  $\log(M_{\text{HI}})$  vs  $\log(M_{*})$ , while the bottom is  $\log(M_{\text{HI}}/M_{*})$  vs  $\log(M_{*})$ . The grey dots in the background are FASHI data, and the black line indicates its average distribution. The red crosses are previously detected HI sources; the green dots are new FUMaS detections with known-redshift optical counterparts; and the blue stars are those without known-redshift optical counterparts.

The last of the three brightest lenticular galaxies is NGC 3998, which has a disturbed and more fragmented HI gas distribution. As shown in Figure 13, the gas disks of the galaxies in the NGC 3998 system are all very irregular. There is a large gas blob without an optical counterpart just north of NGC 3998, consistent with previous observations (Frank et al. 2016). There appear to be signs of interaction between NGC 3990 and NGC 3972, which have tails that extend towards each other. NGC 3982 also has a tail to the southeast. Due to the fragmentation of the gas, the gas distribution in this system is shown in the catalog as separate forms rather than as a complex. The northern gas cloud and

**Table 3.** HI properties of components in complexes.

Name	Flux (Jy km s <sup>-1</sup> )	$\log M(M_{\odot})$
NGC 3992	103.911	9.9
UGC 6969	7.849	8.7
UGC 6940	2.619	8.3
UGC 6923	13.144	9
NGC 4026	2.575	8.3
UGC 6956	14.227	9
NGC 4026 filament	11.67	8.9
NGC 4111	8.34	8.8
NGC 4117	2.992	8.3
NGC 4118	0.732	7.7
UGC 7089	16.912	9.1
UGC 7094	5.601	8.6
NGC 4111 filament	16.71	9.1

UGC 6919 are not listed in our catalog due to their high velocities.

## 5. HI MASS FUNCTION

The number density function describing the HI mass of galaxies can be expressed as:

$$\phi(M_{\text{HI}}) = \frac{dN_{\text{gal}}}{dV d\log_{10}(M_{\text{HI}})}, \quad (4)$$

where  $dN_{\text{gal}}$  is the number of galaxies with HI mass in the logarithmic bin  $d\log_{10}(M_{\text{HI}})$  within the volume  $dV$ . In order to accurately calculate the HIMF of the UMa cluster galaxies, it is important to distinguish the mass of individual galaxies and to determine the volume range. In the catalog of this paper, the majority of HI sources correspond to single galaxies, except for three binary confusions and three complexes. We roughly distinguish the three complexes into individual galaxies, whose properties are shown in Table 3. The three binary confusions, on the other hand, have indistinguishable masses of individual galaxies, which may bias the HIMF. In addition, detections without known-redshift optical counterparts could be clouds rather than galaxies, which would also bias the HIMF, but whether they are galaxies or clouds is difficult to determine, so they are still included in the calculations. Fortunately, the number of confusions and suspected clouds is small and has a limited effect on the results. For the selection of distances and volumes, we used the same strategy as in Busekool et al. (2021), i.e., the masses of the galaxies were all calculated using an average distance of 17.4 Mpc from the UMa cluster, and the depth range was based on the Cosmic Flows 2 of 14.7-21.6 Mpc. Combined with the projected radius of the UMa region of



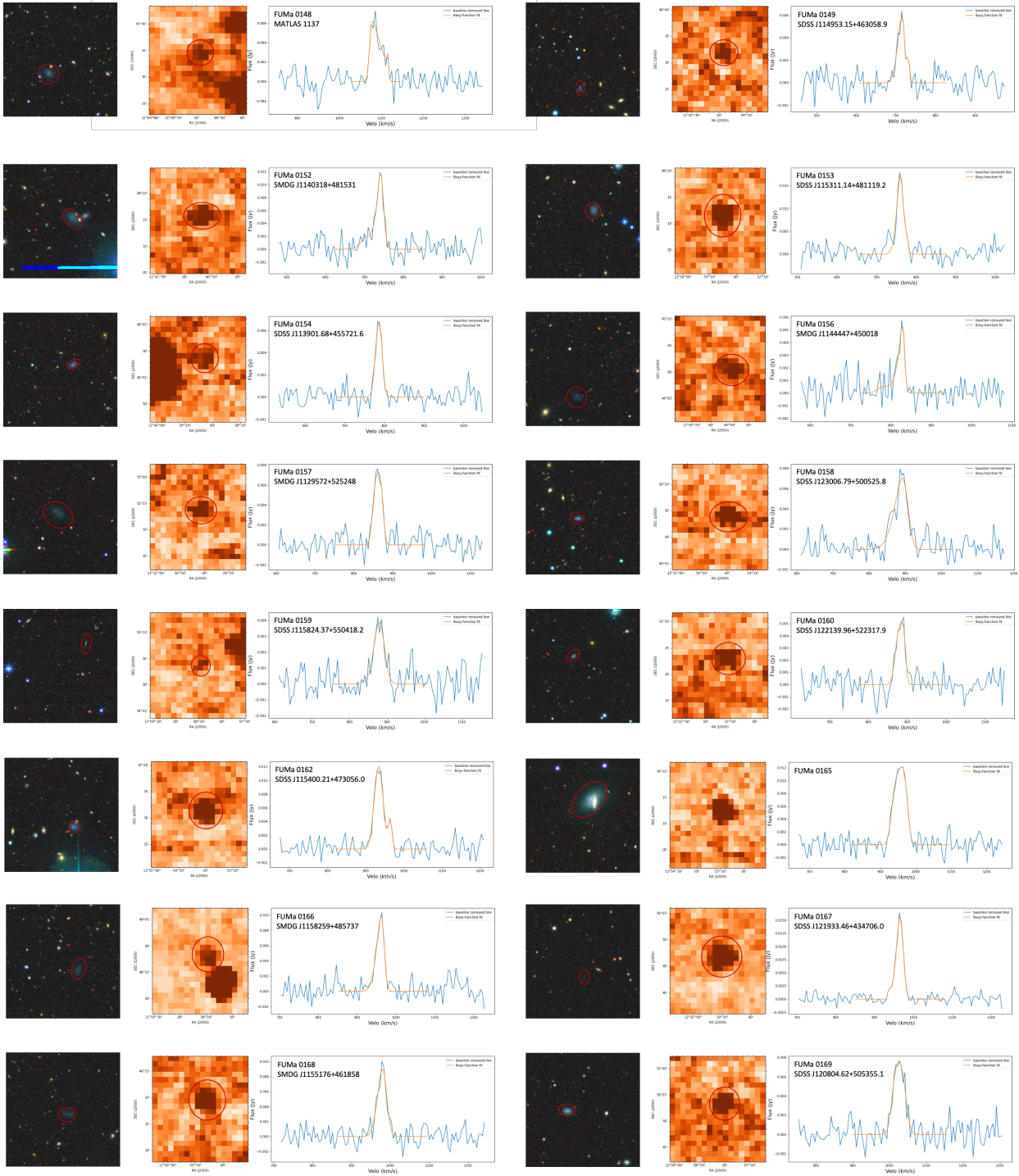


**Figure 9.** Legacy surveys DR10 multicolor images, moment-0 maps and profiles for 25 HI sources with unknown-redshift possible optical counterparts. The Legacy survey images are centered on the location of the HI sources and have a range of about  $3 \times 3$  arcmin<sup>2</sup>. The red circles mark possible optical galaxies. The range of the HI sources are indicated in the moment-0 maps. The HI profile maps contain the names of the detections and optical counterparts, the baseline removed profiles and the barys-function fitted profiles.

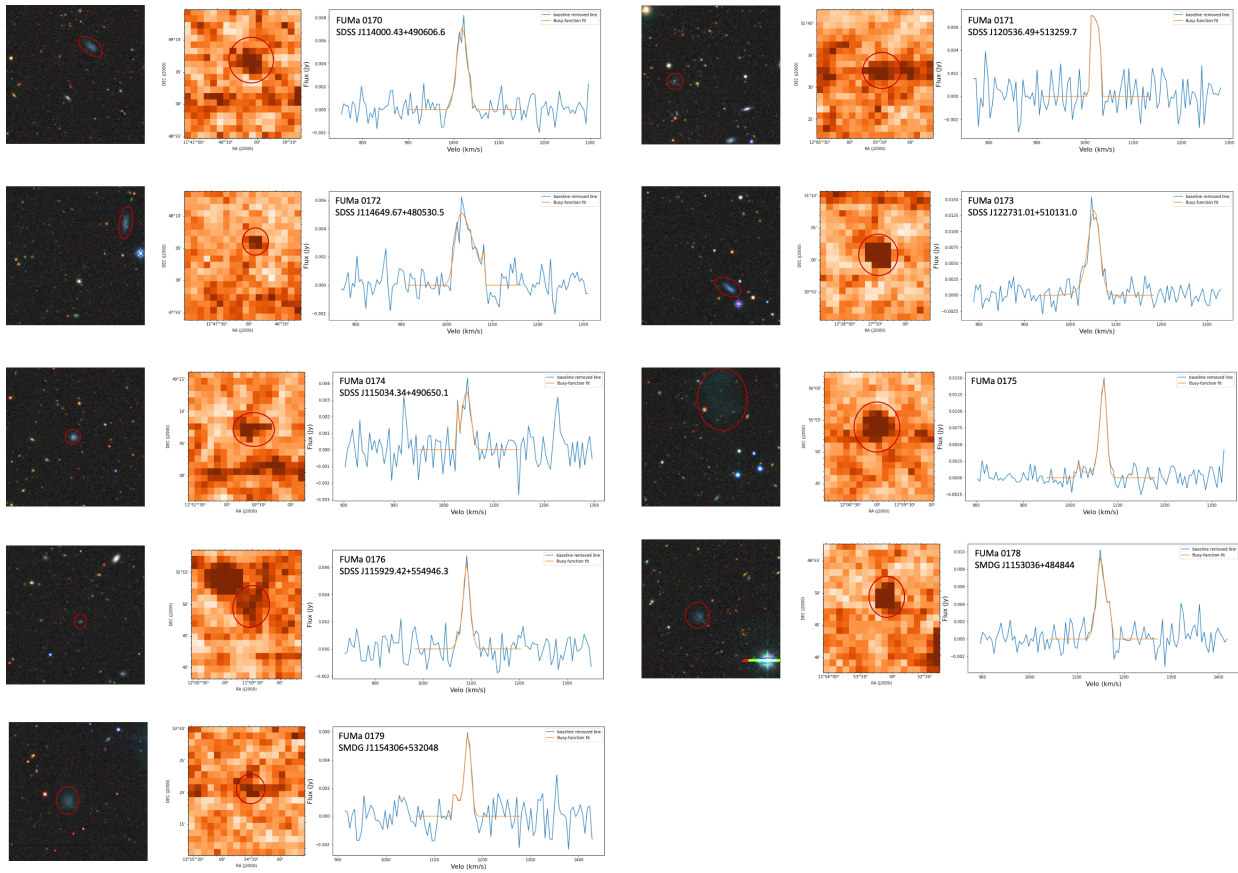
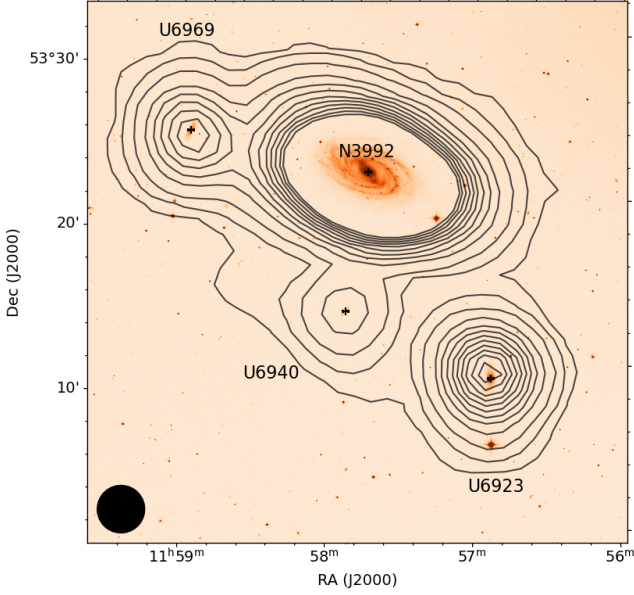


Figure 9. (continued)



**Figure 10.** HI column density contours integrated over 500-1500 km s<sup>-1</sup> overlaid on the DSS B-band optical image. The contour levels are 6, 12, 24, 48, 72, 96, 120, 144, 168, 192, 216, and 240 × 10<sup>18</sup> cm<sup>-2</sup>. The optical centers of N3992 and its three companion galaxies are marked as crosses. The HPBW of FAST is indicated at the bottom-left corner.

7.5 degrees, the volume of the region was calculated to be 123.65 Mpc<sup>3</sup> using the formula:

$$V = \frac{1}{3}\Omega(d_{\max}^3 - d_{\min}^3). \quad (5)$$

The current calculation of the HIMF is based on two main methods, the 1/V<sub>max</sub> method (Schmidt 1968) and the 2-dimensional stepwise maximum likelihood estimator (2DSWML, Efsthathiou et al. 1988). The latter can avoid the influence of LSS but will introduce more errors for small sample data. For the UMa cluster, the 1/V<sub>max</sub> method is more appropriate. The principle of this method is to calculate the maximum volume V<sub>max</sub> of each galaxy that can be detected. In order to calculate the maximum volume, we should first calculate the maximum distance of the galaxies, D<sub>max</sub>, at which each galaxy mass can be detected on its noise scale. For this noise scale, we chose the same parameter as in SoFiA, 4σ<sub>s</sub>. It is worth noting that this distance is limited to 14.7-21.6 Mpc. If D<sub>max</sub> exceeds 21.6 Mpc, the value 21.6 Mpc will be taken. Then the maximum volume between 14.7 and D<sub>max</sub> is calculated by equation 5. The final fit is performed by the following Schechter function:

$$\phi(M_{\text{HI}}) = \ln(10)\phi_* \left(\frac{M_{\text{HI}}}{M_*}\right)^{\alpha+1} e^{-\left(\frac{M_{\text{HI}}}{M_*}\right)}, \quad (6)$$

where φ<sub>\*</sub> is the normalisation constant, α is the low mass slope and M<sub>\*</sub> is the characteristic mass. Due to the low

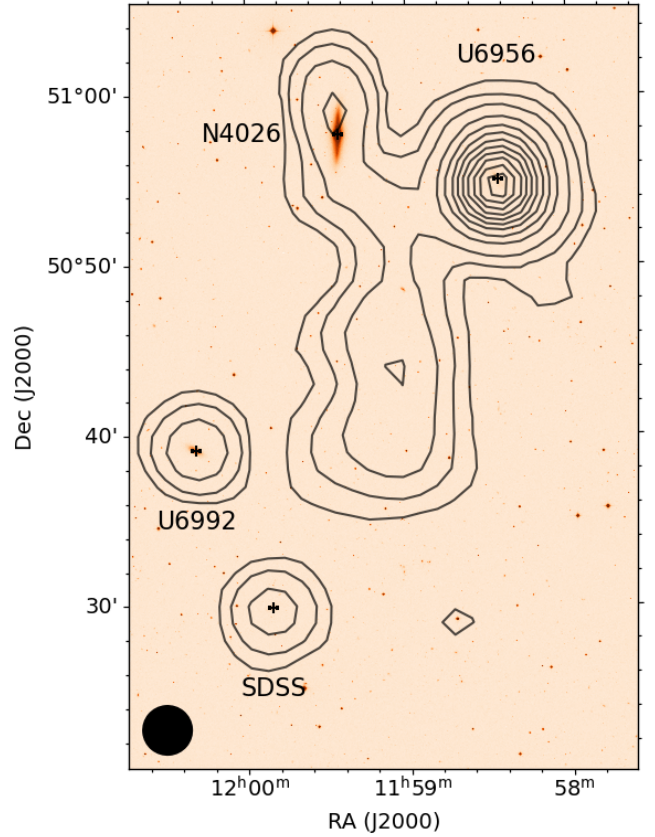


**Figure 11.** HI column density contours are overlaid on the DSS b-band optical image with an integrated range of 600-1400 km s<sup>-1</sup>. The values of the contours are consistent with Figure 10. The crosses in the figure indicate the optical centers of the galaxies. The beam size of FAST is indicated in the bottom-left corner.

completeness of the low mass detections, we filtered out 8 detections with masses less than 10<sup>6.9</sup> M<sub>⊙</sub>. The non-linear least squares (NLLS) method is widely used for fitting. We binned the samples at 0.2 dex width and fitted using the LMFIT package<sup>4</sup>. Still, the selection and width of the bins can affect the results of the fitted parameters, particularly for small sample sizes. We therefore carried out another fitting using the modified maximum likelihood (MML) method (Obreschkow et al. 2018), which is a more robust method that does not require the bins to be split and takes the mass error into account.

The results of the fit are shown in Figure 14, with the top panel showing the HIMF fitted by the NLLS and MML method, and the bottom panel showing a histogram of the galaxy number distribution. The best-fit parameters based on the NLLS method are

<sup>4</sup> <https://lmfit.github.io/lmfit-py/>

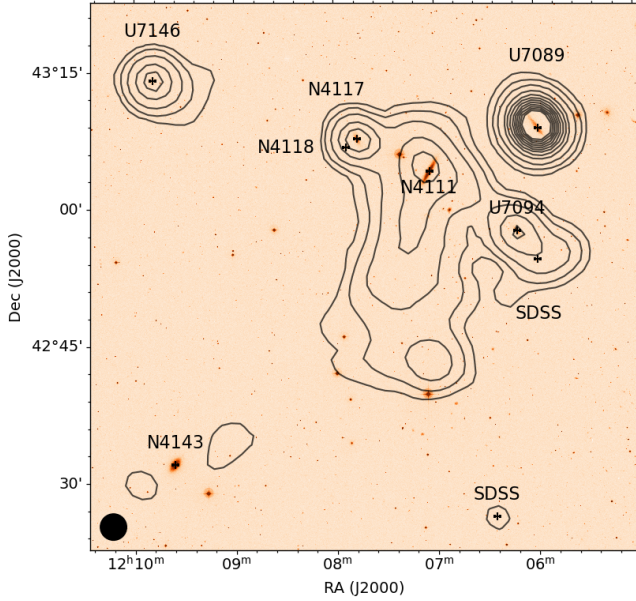


**Figure 12.** HI column density contours are overlaid on the DSS b-band optical image with an integrated range of 500-1300  $\text{km s}^{-1}$ . The values of the contours are consistent with Figure 10. The crosses in the figure indicate the optical centers of the galaxies. The beam size of FAST is indicated at the bottom-left corner.

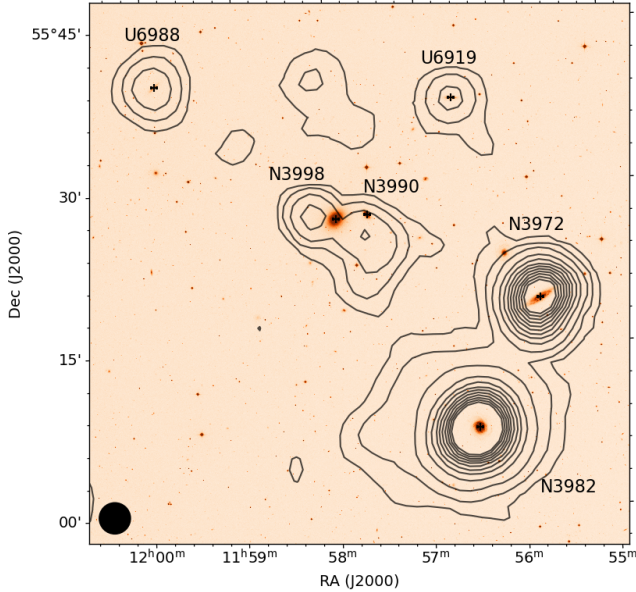


**Figure 13.** HI column density contours are overlaid on the DSS b-band optical image with an integrated range of 550-1500  $\text{km s}^{-1}$ . The values of the contours are consistent with Figure 10. The crosses in the figure indicate the optical centers of the galaxies. The beam size of FAST is indicated at the bottom-left corner.

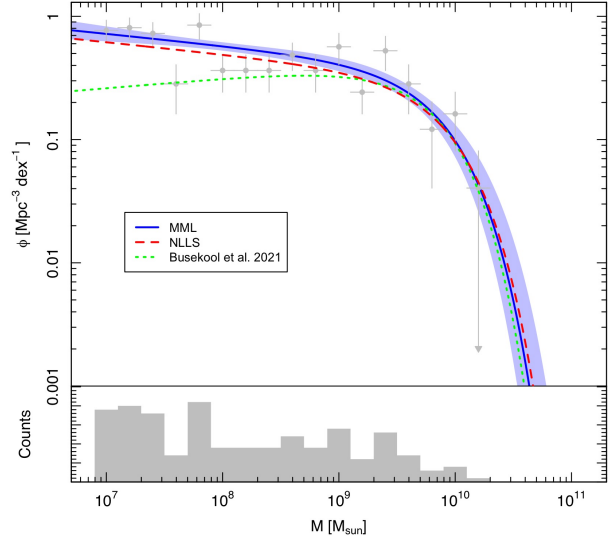


**Figure 14.** The top panel shows the HIMF of the UMA cluster. The grey points with error bars are the number densities within each bin. The curve fitted by the MML method is the blue solid line, with the 1- $\sigma$  uncertainty in the blue area. The red dashed line is the best fit from the LMFIT package based on the NLLS method. The result in Busekool et al. (2021) is shown with the green dotted line. The lower panel shows a histogram of the galaxy number distribution.

$\log_{10}(\phi_*/\text{Mpc}^{-3}) = -0.86 \pm 0.18$ ,  $\alpha = -1.10 \pm 0.08$  and  $\log_{10}(M_*/M_\odot) = 9.92 \pm 0.23$ , and  $\log_{10}(\phi_*/\text{Mpc}^{-3}) = -0.78 \pm 0.11$ ,  $\alpha = -1.10 \pm 0.05$  and  $\log_{10}(M_*/M_\odot) = 9.88 \pm 0.14$  for the MML method. Compared to the blind survey of the VLA ( $\alpha = -0.92 \pm 0.16$  and  $\log_{10}(M_*/M_\odot) = 9.8 \pm 0.8$ ), the slope at the low mass end of our HIMF is steeper, but still not as steep as that of the large blind surveys of HIPASS and ALFALFA. The characteristic mass is more consistent. This result is due to a large number of new FUMaS detections of galaxies with masses concentrated at  $10^7$ - $10^8 M_\odot$ , raising the slope at the low-mass end. Our finding of a flatter slope compared to the global HIMFs is in agreement with the conclusions of several investigators that the low-mass slope is flatter in galaxy density environments (Rosenberg & Schneider 2002; Springob et al. 2005; Pisano et al. 2011; Westmeier et al. 2017; Said et al. 2019; Jones et al. 2020), suggesting that the environment affects the HIMF. This is also consistent with theoretical predictions that galaxies in high-density regions are more likely to interact with each other thus HI gas is stripped away and fewer low-mass galaxies are detected. Note that the slope of our HIMF is almost identical to that of the optical LF found by Trentham et al. (2001), which suggests that the gas stripping process is dominated by tidal strip-

ping rather than ram pressure in the UMa cluster, as ram pressure effect should produce more gas poor dwarf galaxies and resulting in different slopes between the LF and HIMF (Trentham et al. 2001; Busekool et al. 2021). This result is also consistent with the fact that the UMa cluster has not hot X-ray halo thus ram pressure stripping by hot gas is negligible.

## 6. CONCLUSIONS

The UMa cluster is an ideal target for studying the evolution of dwarf galaxies, galactic interactions, and environmental influences on the HIMF, but it has not been explored thoroughly and lacks a complete HI source catalog. The FAST HI survey of the UMa cluster is our first attempt to conduct a complete blind HI survey of the UMa region. The main results are summarized as follows:

1. Using SoFiA for source finding and combining with manual search, we have obtained the most complete HI source catalog for the UMa cluster. This catalog contains 179 HI sources with velocities in the range 625-1213.4 km s<sup>-1</sup> and masses in the range 10<sup>6.0</sup>-10<sup>10.1</sup> M<sub>⊙</sub> assuming a unity distance of 17.4 Mpc. Compared to the previous UMa catalogs, we have detected all the HI sources previously reported in the literature, and also detect HI signals for the vast majority of galaxies in the optical catalog (151 out of 166 galaxies in Pak et al. (2014)).

2. There are 55 HI sources in the catalog that are detected for the first time. In addition, 32 detections have no optical redshifts, for which 25 of them have corresponding galaxies in optical images, while the remaining 7 are most likely HI clouds without optical counterparts. The high sensitivity of FAST can provide a good comple-

ment to optical observations, conferring redshift information on dwarf galaxies and increasing galaxy cluster members.

3. There are many interacting systems in the UMa cluster, and our catalog contains three binary confusions and three complexes. We describe the four interaction regions in details. NGC 3992 and its three companion galaxies have overlapping gas disks but do not appear to interact strongly; there is a filament of 142 kpc between NGC 4026 and SDSS J115950.81+502955.3, and a filament of 152 kpc extended out side NGC 4111; and there are several fragmented gas structures in the NGC3998 system and NGC 4111 complex.

4. We computed the HIMF of the UMa cluster using the 1/V<sub>max</sub> method and fitted it with both the NLLS and MML methods. The best-fit parameters are log<sub>10</sub>(ϕ<sub>\*</sub>/Mpc<sup>-3</sup>) = -0.86 ± 0.18, α = -1.10 ± 0.08 and log<sub>10</sub>(M<sub>\*</sub>/M<sub>⊙</sub>) = 9.92 ± 0.23 for the NLLS method, and log<sub>10</sub>(ϕ<sub>\*</sub>/Mpc<sup>-3</sup>) = -0.78 ± 0.11, α = -1.10 ± 0.05 and log<sub>10</sub>(M<sub>\*</sub>/M<sub>⊙</sub>) = 9.88 ± 0.14 for the MML method. Compared to the VLA HIMF, the characteristic mass is consistent at the high-mass end, but the slope is steeper at the low-mass end because we detected more low-mass galaxies. Compared to the global HIMF, we find a flatter slope at the low-mass end, suggesting that gas stripping due to interactions in high-density galaxy regions reduces the number density of low-mass galaxies. Such scenario is consistent with theoretical predictions for galaxy evolutions in cluster environments.

This work is supported by the Guizhou Provincial Science and Technology Projects (QKHFQ[2023]003, QKHPTRC-ZDSYS[2023]003, QKHFQ[2024]001-1)

## REFERENCES

- Ahumada, R., Allende Prieto, C., Almeida, A., et al. 2020, *ApJS*, 249, 3, doi: [10.3847/1538-4365/ab929e](https://doi.org/10.3847/1538-4365/ab929e)
- Appleton, P. N. 1983, *MNRAS*, 203, 533, doi: [10.1093/mnras/203.2.533](https://doi.org/10.1093/mnras/203.2.533)
- Baek, S.-J., Park, A., Ahn, Y.-J., & Choo, J. 2015, *The Analyst*, 140, 250, doi: [10.1039/C4AN01061B](https://doi.org/10.1039/C4AN01061B)
- Barnes, D. G., Staveley-Smith, L., de Blok, W. J. G., et al. 2001, *MNRAS*, 322, 486, doi: [10.1046/j.1365-8711.2001.04102.x](https://doi.org/10.1046/j.1365-8711.2001.04102.x)
- Beers, T. C., Flynn, K., & Gebhardt, K. 1990, *AJ*, 100, 32, doi: [10.1086/115487](https://doi.org/10.1086/115487)
- Bell, E. F., McIntosh, D. H., Katz, N., & Weinberg, M. D. 2003, *ApJS*, 149, 289, doi: [10.1086/378847](https://doi.org/10.1086/378847)
- Benitez-Llambay, A., & Frenk, C. 2020, *MNRAS*, 498, 4887, doi: [10.1093/mnras/staa2698](https://doi.org/10.1093/mnras/staa2698)
- Blanton, M. R., Dalcanton, J., Eisenstein, D., et al. 2001, *AJ*, 121, 2358, doi: [10.1086/320405](https://doi.org/10.1086/320405)
- Blanton, M. R., Hogg, D. W., Bahcall, N. A., et al. 2003, *ApJ*, 592, 819, doi: [10.1086/375776](https://doi.org/10.1086/375776)
- Bottema, R. 2002, *A&A*, 388, 809, doi: [10.1051/0004-6361:20020541](https://doi.org/10.1051/0004-6361:20020541)
- Bottema, R., & Verheijen, M. A. W. 2002, *A&A*, 388, 793, doi: [10.1051/0004-6361:20020539](https://doi.org/10.1051/0004-6361:20020539)
- Bull, P., Akrami, Y., Adamek, J., et al. 2016, *Physics of the Dark Universe*, 12, 56, doi: [10.1016/j.dark.2016.02.001](https://doi.org/10.1016/j.dark.2016.02.001)
- Busekool, E., Verheijen, M. A. W., van der Hulst, J. M., et al. 2021, *MNRAS*, 501, 2608, doi: [10.1093/mnras/staa3582](https://doi.org/10.1093/mnras/staa3582)
- Chandola, Y., Li, D., Tsai, C.-W., et al. 2024, *MNRAS*, 527, 603, doi: [10.1093/mnras/stad3018](https://doi.org/10.1093/mnras/stad3018)

- Courtois, H. M., & Tully, R. B. 2015, *MNRAS*, 447, 1531, doi: [10.1093/mnras/stu2405](https://doi.org/10.1093/mnras/stu2405)
- Dunning, A., Bowen, M., Castillo, S., et al. 2017, in 2017 XXXIInd General Assembly and Scientific Symposium of the International Union of Radio Science (URSI GASS), 1–4, doi: [10.23919/URSIGASS.2017.8105012](https://doi.org/10.23919/URSIGASS.2017.8105012)
- Efstathiou, G., Ellis, R. S., & Peterson, B. A. 1988, *MNRAS*, 232, 431, doi: [10.1093/mnras/232.2.431](https://doi.org/10.1093/mnras/232.2.431)
- Fouque, P., Durand, N., Bottinelli, L., Gouguenheim, L., & Paturel, G. 1990, *A&AS*, 86, 473
- Frank, B. S., Morganti, R., Oosterloo, T., Nyland, K., & Serra, P. 2016, *A&A*, 592, A94, doi: [10.1051/0004-6361/201628282](https://doi.org/10.1051/0004-6361/201628282)
- Freeland, E., Stilp, A., & Wilcots, E. 2009, *AJ*, 138, 295, doi: [10.1088/0004-6256/138/1/295](https://doi.org/10.1088/0004-6256/138/1/295)
- Giovanelli, R., & Haynes, M. P. 2015, *A&A Rv*, 24, 1, doi: [10.1007/s00159-015-0085-3](https://doi.org/10.1007/s00159-015-0085-3)
- Giovanelli, R., Haynes, M. P., Kent, B. R., et al. 2005, *AJ*, 130, 2598, doi: [10.1086/497431](https://doi.org/10.1086/497431)
- Gottesman, S. T., Ball, R., Hunter, J. H., J., & Huntley, J. M. 1984, *ApJ*, 286, 471, doi: [10.1086/162622](https://doi.org/10.1086/162622)
- Haynes, M. P., Giovanelli, R., Kent, B. R., et al. 2018, *ApJ*, 861, 49, doi: [10.3847/1538-4357/aac956](https://doi.org/10.3847/1538-4357/aac956)
- Huchtmeier, W. K., Petrosian, A., Gopal-Krishna, & Kunth, D. 2007, *A&A*, 462, 919, doi: [10.1051/0004-6361:20065712](https://doi.org/10.1051/0004-6361:20065712)
- Jenkins, A., Frenk, C. S., White, S. D. M., et al. 2001, *MNRAS*, 321, 372, doi: [10.1046/j.1365-8711.2001.04029.x](https://doi.org/10.1046/j.1365-8711.2001.04029.x)
- Jiang, P., Yue, Y., Gan, H., et al. 2019, *Science China Physics, Mechanics, and Astronomy*, 62, 959502, doi: [10.1007/s11433-018-9376-1](https://doi.org/10.1007/s11433-018-9376-1)
- Jiang, P., Tang, N.-Y., Hou, L.-G., et al. 2020, *Research in Astronomy and Astrophysics*, 20, 064, doi: [10.1088/1674-4527/20/5/64](https://doi.org/10.1088/1674-4527/20/5/64)
- Jing, Y., Wang, J., Xu, C., et al. 2024, *Science China Physics, Mechanics, and Astronomy*, 67, 259514, doi: [10.1007/s11433-023-2333-8](https://doi.org/10.1007/s11433-023-2333-8)
- Jones, M. G., Haynes, M. P., Giovanelli, R., & Moorman, C. 2018, *MNRAS*, 477, 2, doi: [10.1093/mnras/sty521](https://doi.org/10.1093/mnras/sty521)
- Jones, M. G., Hess, K. M., Adams, E. A. K., & Verdes-Montenegro, L. 2020, *MNRAS*, 494, 2090, doi: [10.1093/mnras/staa810](https://doi.org/10.1093/mnras/staa810)
- Jones, M. G., Papastergis, E., Haynes, M. P., & Giovanelli, R. 2016, *MNRAS*, 457, 4393, doi: [10.1093/mnras/stw263](https://doi.org/10.1093/mnras/stw263)
- Koribalski, B. S., Staveley-Smith, L., Kilborn, V. A., et al. 2004, *AJ*, 128, 16, doi: [10.1086/421744](https://doi.org/10.1086/421744)
- Kravtsov, A. V., Gnedin, O. Y., & Klypin, A. A. 2004, *ApJ*, 609, 482, doi: [10.1086/421322](https://doi.org/10.1086/421322)
- Maddox, N., Frank, B. S., Ponomareva, A. A., et al. 2021, *A&A*, 646, A35, doi: [10.1051/0004-6361/202039655](https://doi.org/10.1051/0004-6361/202039655)
- Martin, A. M., Papastergis, E., Giovanelli, R., et al. 2010, *ApJ*, 723, 1359, doi: [10.1088/0004-637X/723/2/1359](https://doi.org/10.1088/0004-637X/723/2/1359)
- Meyer, M. J., Zwaan, M. A., Webster, R. L., et al. 2004, *MNRAS*, 350, 1195, doi: [10.1111/j.1365-2966.2004.07710.x](https://doi.org/10.1111/j.1365-2966.2004.07710.x)
- Moorman, C. M., Vogeley, M. S., Hoyle, F., et al. 2014, *MNRAS*, 444, 3559, doi: [10.1093/mnras/stu1674](https://doi.org/10.1093/mnras/stu1674)
- Obreschkow, D., Murray, S. G., Robotham, A. S. G., & Westmeier, T. 2018, *MNRAS*, 474, 5500, doi: [10.1093/mnras/stx3155](https://doi.org/10.1093/mnras/stx3155)
- O’Neil, K., Schneider, S. E., van Driel, W., et al. 2023, *AJ*, 165, 263, doi: [10.3847/1538-3881/acd345](https://doi.org/10.3847/1538-3881/acd345)
- Pak, M., Rey, S.-C., Lisker, T., et al. 2014, *MNRAS*, 445, 630, doi: [10.1093/mnras/stu1722](https://doi.org/10.1093/mnras/stu1722)
- Paturel, G., Theureau, G., Bottinelli, L., et al. 2003, *A&A*, 412, 57, doi: [10.1051/0004-6361:20031412](https://doi.org/10.1051/0004-6361:20031412)
- Pisano, D. J., Barnes, D. G., Staveley-Smith, L., et al. 2011, *ApJS*, 197, 28, doi: [10.1088/0067-0049/197/2/28](https://doi.org/10.1088/0067-0049/197/2/28)
- Ponomareva, A. A., Jarvis, M. J., Pan, H., et al. 2023, *MNRAS*, 522, 5308, doi: [10.1093/mnras/stad1249](https://doi.org/10.1093/mnras/stad1249)
- Poulain, M., Marleau, F. R., Habas, R., et al. 2022, *A&A*, 659, A14, doi: [10.1051/0004-6361/202142012](https://doi.org/10.1051/0004-6361/202142012)
- Qian, L., Yao, R., Sun, J., et al. 2020, *The Innovation*, 1, 100053, doi: [10.1016/j.xinn.2020.100053](https://doi.org/10.1016/j.xinn.2020.100053)
- Rosenberg, J. L., & Schneider, S. E. 2002, *ApJ*, 567, 247, doi: [10.1086/338377](https://doi.org/10.1086/338377)
- Said, K., Kraan-Korteweg, R. C., & Staveley-Smith, L. 2019, *MNRAS*, 486, 1796, doi: [10.1093/mnras/stz956](https://doi.org/10.1093/mnras/stz956)
- Schechter, P. 1976, *ApJ*, 203, 297, doi: [10.1086/154079](https://doi.org/10.1086/154079)
- Schmidt, M. 1968, *ApJ*, 151, 393, doi: [10.1086/149446](https://doi.org/10.1086/149446)
- Serra, P., Oosterloo, T., Morganti, R., et al. 2012, *MNRAS*, 422, 1835, doi: [10.1111/j.1365-2966.2012.20219.x](https://doi.org/10.1111/j.1365-2966.2012.20219.x)
- Serra, P., Westmeier, T., Giese, N., et al. 2015, *MNRAS*, 448, 1922, doi: [10.1093/mnras/stv079](https://doi.org/10.1093/mnras/stv079)
- Spergel, D. N., & Steinhardt, P. J. 2000, *PhRvL*, 84, 3760, doi: [10.1103/PhysRevLett.84.3760](https://doi.org/10.1103/PhysRevLett.84.3760)
- Springob, C. M., Haynes, M. P., & Giovanelli, R. 2005, *ApJ*, 621, 215, doi: [10.1086/427432](https://doi.org/10.1086/427432)
- Stierwalt, S., Haynes, M. P., Giovanelli, R., et al. 2009, *AJ*, 138, 338, doi: [10.1088/0004-6256/138/2/338](https://doi.org/10.1088/0004-6256/138/2/338)
- Trentham, N., Tully, R. B., & Verheijen, M. A. W. 2001, *MNRAS*, 325, 385, doi: [10.1046/j.1365-8711.2001.04427.x](https://doi.org/10.1046/j.1365-8711.2001.04427.x)
- Tully, R. B., & Courtois, H. M. 2012, *ApJ*, 749, 78, doi: [10.1088/0004-637X/749/1/78](https://doi.org/10.1088/0004-637X/749/1/78)
- Tully, R. B., Verheijen, M. A. W., Pierce, M. J., Huang, J.-S., & Wainscoat, R. J. 1996, *AJ*, 112, 2471, doi: [10.1086/118196](https://doi.org/10.1086/118196)
- van Driel, W., Davies, R. D., & Appleton, P. N. 1988, *A&A*, 199, 41

- van Driel, W., Butcher, Z., Schneider, S., et al. 2016, *A&A*, 595, A118, doi: [10.1051/0004-6361/201528048](https://doi.org/10.1051/0004-6361/201528048)
- Verde, L., Oh, S. P., & Jimenez, R. 2002, *MNRAS*, 336, 541, doi: [10.1046/j.1365-8711.2002.05771.x](https://doi.org/10.1046/j.1365-8711.2002.05771.x)
- Verheijen, M. A. W., & Sancisi, R. 2001, *A&A*, 370, 765, doi: [10.1051/0004-6361:20010090](https://doi.org/10.1051/0004-6361:20010090)
- Westmeier, T., Jurek, R., Obreschkow, D., Koribalski, B. S., & Staveley-Smith, L. 2014, *MNRAS*, 438, 1176, doi: [10.1093/mnras/stt2266](https://doi.org/10.1093/mnras/stt2266)
- Westmeier, T., Obreschkow, D., Calabretta, M., et al. 2017, *MNRAS*, 472, 4832, doi: [10.1093/mnras/stx2289](https://doi.org/10.1093/mnras/stx2289)
- Westmeier, T., Kitaeff, S., Pallot, D., et al. 2021, *MNRAS*, 506, 3962, doi: [10.1093/mnras/stab1881](https://doi.org/10.1093/mnras/stab1881)
- White, S. D. M., & Rees, M. J. 1978, *MNRAS*, 183, 341, doi: [10.1093/mnras/183.3.341](https://doi.org/10.1093/mnras/183.3.341)
- Wolfinger, K., Kilborn, V. A., Koribalski, B. S., et al. 2013, *MNRAS*, 428, 1790, doi: [10.1093/mnras/sts160](https://doi.org/10.1093/mnras/sts160)
- Xu, J.-L., Zhang, C.-P., Yu, N., et al. 2021, *ApJ*, 922, 53, doi: [10.3847/1538-4357/ac26b7](https://doi.org/10.3847/1538-4357/ac26b7)
- Yu, H., Zhu, M., Xu, J.-L., et al. 2023, *MNRAS*, 521, 2719, doi: [10.1093/mnras/stad436](https://doi.org/10.1093/mnras/stad436)
- Zaritsky, D., Donnerstein, R., Dey, A., et al. 2023, *ApJS*, 267, 27, doi: [10.3847/1538-4365/acdd71](https://doi.org/10.3847/1538-4365/acdd71)
- Zhang, C.-P., Zhu, M., Jiang, P., et al. 2024, *Science China Physics, Mechanics, and Astronomy*, 67, 219511, doi: [10.1007/s11433-023-2219-7](https://doi.org/10.1007/s11433-023-2219-7)
- Zhou, R., Zhu, M., Yang, Y., et al. 2023, *ApJ*, 952, 130, doi: [10.3847/1538-4357/acdcf5](https://doi.org/10.3847/1538-4357/acdcf5)
- Zwaan, M. A., Briggs, F. H., Sprayberry, D., & Sorar, E. 1997, *ApJ*, 490, 173, doi: [10.1086/304872](https://doi.org/10.1086/304872)
- Zwaan, M. A., Meyer, M. J., Staveley-Smith, L., & Webster, R. L. 2005, *MNRAS*, 359, L30, doi: [10.1111/j.1745-3933.2005.00029.x](https://doi.org/10.1111/j.1745-3933.2005.00029.x)
- Zwaan, M. A., Staveley-Smith, L., Koribalski, B. S., et al. 2003, *AJ*, 125, 2842, doi: [10.1086/374944](https://doi.org/10.1086/374944)